Check for updates

JGR Atmospheres

RESEARCH ARTICLE
10.1029/2021JD035446

Microphysical Characteristics of the Coexisting Frontal and Warm-Sector Heavy Rainfall in South China

Bin Han[1,2,3,4], **Yu Du**[1,2,3,4], **Chong Wu**[5], **and Xi Liu**[6]

[1]School of Atmospheric Sciences, Sun Yat-sen University, Zhuhai, China, [2]Southern Marine Science and Engineering Guangdong Laboratory (Zhuhai), Zhuhai, China, [3]Guangdong Province Key Laboratory for Climate Change and Natural Disaster Studies, Sun Yat-sen University, Zhuhai, China, [4]Key Laboratory of Tropical Atmosphere-Ocean System, Ministry of Education, Sun Yat-sen University, Zhuhai, China, [5]State Key Lab of Severe Weather, Chinese Academy of Meteorological Sciences, Beijing, China, [6]Nanjing Joint Institute for Atmospheric Sciences, Nanjing, China

Abstract Inland frontal heavy rainfall (FR) and coastal warm-sector heavy rainfall (WR) are two typical types of precipitation in South China during the pre-summer rainy season. FR and WR are found to be generated by different mechanisms, but their differences in microphysical features and relevant possible reasons are not well understood. In the present study, dual-polarization observations merged from 10 radars are utilized to investigate microphysical characteristics of two coexisting convective systems producing FR and WR. Overall, the WR has a stronger convection intensity, larger raindrop size, and higher liquid water content than the FR. The larger raindrops might be partly attributed to the deeper warm-sector convection evidenced by stronger convective updrafts, which could potentially promote mixed-phase processes. Raindrops in the WR are still larger even when the WR has a similar convection intensity with the FR, which might be explained by the active warm rain processes associated with higher low-level humidity and more evident low-level rotation in the WR. In addition, the FR was originally developed near the front and then vacated from the front into the warm sector, exhibiting an obvious temporal evolution in microphysical characteristics. Despite weaker convection intensity, the FR away from the front manifests a larger mean raindrop size than the FR near the front possibly because of more abundant environmental moisture in the warm sector.

Key Points:

- The warm-sector convection has a stronger convection intensity, larger raindrop size, and higher liquid water content
- The larger raindrop size in the warm-sector heavy rainfall is possibly due to higher low-level humidity and more evident low-level rotation
- The frontal heavy rainfall exhibits a temporal evolution in microphysical characteristics

Correspondence to:
Y. Du,
duyu7@mail.sysu.edu.cn

Citation:
Han, B., Du, Y., Wu, C., & Liu, X. (2021). Microphysical characteristics of the coexisting frontal and warm-sector heavy rainfall in South China. *Journal of Geophysical Research: Atmospheres*, *126*, e2021JD035446. https://doi.org/10.1029/2021JD035446

Received 21 JUN 2021
Accepted 8 OCT 2021

© 2021. American Geophysical Union. All Rights Reserved.

1. Introduction

South China, located in the north of the South China Sea and at relatively low latitudes, is often influenced by warm and moist air from the sea, which is one of the regions where heavy rainfall frequently occurs. Several field campaigns were carried out during the past 40 years, and mainly focused on the mechanisms of the initiation and maintenance of heavy rainfall over South China (e.g., Huang, 1986; Luo et al., 2017; Zhang et al., 2011; Zhou, 2003). Findings from these field campaigns have greatly advanced our understanding of the dynamics and thermodynamics of heavy rainfall in South China. During the pre-summer rainy season (April-June), two types of heavy rainfall generally exist: one is near the synoptic-scale cold front [i.e., frontal heavy rainfall (FR)] established by the convergence of cold-dry-northerly airflows and warm-moist-southerly airflows (Ding, 1994; Zhao et al., 2007); the other one occurs more than 200 km ahead of the front in the warm sector [i.e., warm-sector heavy rainfall (WR)] and at coasts without obvious synoptic forcing (Huang, 1986; Lin et al., 2006).

Both FR and WR can cause severe economic damage and life losses. Sometimes, heavy rainfall in South China during the pre-summer rainy season is characterized by coexisting inland frontal rainband and coastal warm-sector rainband (e.g., Chen et al., 2018; Li & Du, 2021; Li et al., 2020; Liu et al., 2020; Wu et al., 2020). Past studies have shown that FR is related to the dynamical forcing by front lifting at the synoptic scale (e.g., Akiyama, 1973; Tao & Chen, 1987). In contrast, WR in South China is initialized by complex local forcings, including coastal convergence associated with low-level jet (e.g., Du & Chen, 2018, 2019; Du, Chen, Han, Mai, et al., 2020), topographic lifting (e.g., Wang et al., 2014; Du, Chen, Han, Bai, & Li, 2020), land-sea contrast (e.g., Chen et al., 2016; Wu et al., 2020), and cold pools (e.g., Wu & Luo, 2016). Besides, WR frequently occurs in the coastal region that is profoundly affected by southerly warm and moist winds from the ocean with more favorable thermodynamical conditions (Xia et al., 2006). Overall, the differences between these

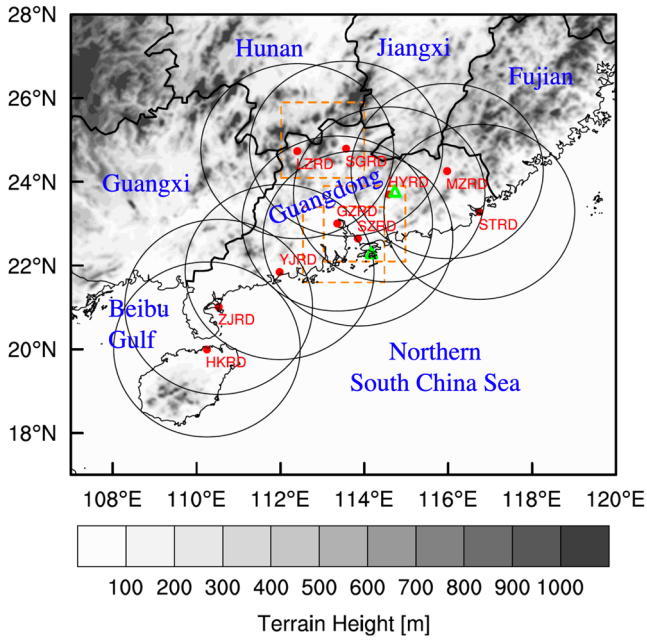

Figure 1. Locations of ten dual-polarization radars in South China (red dots) and terrain height (shaded, units: m). The black circles show the maximum scanning range of radars. The dashed orange boxes represent the dual-Doppler radar wind field retrieval domains. Locations of two sounding sites are shown by the green triangles.

two types of heavy rainfall from the dynamical and thermodynamical perspectives have been well documented in previous studies.

Stronger convective updrafts commonly favor the riming process by lifting more liquid droplets above the freezing level and thus lead to more production of heavily rimed particles like graupel and/or hail. These relationships between the kinematical and microphysical features can be seen in the mesoscale convective system (MCS) evolved from the initial stage to mature stage (e.g., Wen et al., 2017) and also in the comparison between the midlatitude continental MCSs and tropical oceanic MCSs (e.g., Barnes & Houze, 2014; Matsui et al., 2020). The melting of more graupel and/or hail particles usually induces higher initial liquid water content (LWC) just below the melting level. However, the variability of LWC and raindrop size with decreasing height is closely associated with environmental thermodynamical conditions at lower levels (e.g., Lang et al., 2010; Rowe et al., 2011, 2012; Ulbrich & Atlas, 2007). Therefore, as revealed in these studies, it is expected that the differences in the dynamical forcings and thermodynamical conditions between inland FR and coastal WR can cause microphysical differences in the ice-based and warm rain processes, and ultimately result in varying rain microphysics. However, the microphysical differences between these two types of heavy rainfall are still not clear because of limited microphysical observations over South China in the past.

Dual-polarimetric radar can provide additional information such as particle shape, size, and orientation (Bringi & Chandrasekar, 2001; Zrnic & Ryzhkov, 1999), which has been employed widely to study the microphysical features in different kinds of severe convective storms over the world (e.g., Barnes & Houze, 2014; Chen et al., 2019; Kumjian & Ryzhkov, 2008; Matsui et al., 2020; Rowe et al., 2011, 2012; Wen et al., 2017). In South China, due to the lack of polarimetric observations, only a few studies about convective events have been investigated using polarimetric measurements (e.g., Li et al., 2019; Wang et al., 2019; Wu, Zhao, et al., 2018), and they found that active warm-rain processes are the main contributor to the extreme rainfall (Luo et al., 2020). However, these studies either focus on the microphysical structure of the squall line and typhoon or don't strictly distinguish the types of heavy rainfall. During the last few years, multiple operational radars in South China have been upgraded to dual-polarization mode (Zhao et al., 2019). Large spatial coverage and high temporal resolution of polarimetric radar observations provide us a new opportunity to investigate the microphysical characteristics of convective systems producing FR and WR. Therefore, the purpose of the present study is to conduct a comparison between these two types of heavy rainfall from a microphysical perspective. Moreover, we further attempt to explore the possible reasons for the varying microphysical characteristics between the two types of heavy rainfall, which have not been well studied.

This paper focuses on a typical heavy rainfall event during the pre-summer rainy season, featured by the coexisting FR and WR in South China. Data and methodology used in this study are briefly described in Section 2, followed by the case description and environmental conditions in Section 3. The detailed comparison of microphysical characteristics between the two types of convection, as well as the temporal evolution of microphysical features for the frontal convection, are presented in Section 4. The possible causes for the microphysical differences are discussed in Section 5. Summary is provided in Section 6.

2. Data and Methodology

2.1. Data

Polarimetric variables measured from ten S-band dual-polarization radars deployed in South China (Figure 1) are used to examine the microphysical characteristics of the FR and WR in the present event. All the radars operate with nine-elevation Plan Position Indicator (PPI) scans (0.5°, 1.5°, 2.4°, 3.3°, 4.3°, 6.0°, 9.9°,

14.6°, and 19.5°) every 6 min to obtain the full volume coverage. The quality control is proceeded by noise suppression with a 1-km running-average filter (Wu, Liu, et al., 2018). After the quality control, observations from each radar are bilinearly interpolated onto a 3-D Cartesian coordinate. The horizontal resolution is 1 km and the vertical extent is from 0.5 to 15 km above the mean sea level (ASL) with a grid spacing of 0.5 km. Finally, the gridded observational data of 10 radars are merged using the weighted-average method (Zhang et al., 2005):

$$f^m = \sum_{n=1,10} w_n f_n^a \Big/ \sum_{n=1,10} w_n \tag{1}$$

where f^m is the merged data at each grid point, f_n^a is the gridded data of each radar, and w_n is the corresponding weight for each radar. The calculation of w_n follows:

$$w_n = exp\left(-\frac{r^2}{R^2}\right) \tag{2}$$

where r is the distance between the radar and each grid point, and R is the radius of influence. For S-band radars, R is generally taken as 300 km. After data processing, five polarimetric variables including horizontal radar reflectivity (Z_H), differential reflectivity (Z_{DR}), differential phase (Φ_{DP}), specific differential propagation phase (K_{DP}), and correlation coefficient (ρ_{HV}) are employed based on a modified hydrometeor classification algorithm (HCA) as in Wu, Liu, et al. (2018). In this study, the estimation of K_{DP} is derived from a slope of the least-squares fit of the filtered Φ_{DP} (Section 2a in Park et al., 2009). The modified HCA is based on the algorithm described in Park et al. (2009) and is optimized for the Chinese operational S-band radars. 10 dominant categories are identified: (a) ground clutter (GC); (b) biological scatters (BS); (c) dry snow (DS); (d) wet snow (WS); (e) ice crystal (CR); (f) graupel (GR); (g) "big drops" (BD); (h) light and moderate rain (RA); (i) heavy rain (HR); and (j) a mixture of rain and hail (RH). Non-meteorological radar echoes (i.e., GC and BS) are excluded from the data.

To show the temporal evolution of the two coexisting rainbands in South China, we use satellite-based precipitation estimates from the Integrated Multi-satellite Retrievals for GPM (IMERG) Final Run product (Huffman et al., 2019; Tan et al., 2019). The IMERG precipitation data has a high spatial resolution of 0.1° with a time interval of 30 min. The environmental conditions of the present event are analyzed by the European Centre for Medium-Range Weather Forecasts (ECMWF) hourly reanalysis data (ERA5) with a horizontal resolution of 0.25° × 0.25°. Besides, soundings from two stations (i.e., Heyuan and Hong Kong) located ahead of the frontal rainband and warm-sector rainband are selected to further provide additional information about environmental conditions.

2.2. The Calculation of Frontogenesis Function

To identify the location of front objectively, the frontogenesis function is calculated with the ERA5 reanalysis data at the surface layer. The calculation follows Bluestein (1986) as below:

$$F = \frac{d}{dt}\left|\nabla_h \theta_e\right| = F1 + F2 + F3 + F4 \tag{3}$$

$$F1 = -\frac{1}{2}A\left|\nabla_h \theta_e\right| \tag{4}$$

$$F2 = -\frac{1}{2}\left[B\left(\frac{\partial \theta_e}{\partial x}\right)^2 + 2C\left(\frac{\partial \theta_e}{\partial x}\right)\left(\frac{\partial \theta_e}{\partial y}\right) - B\left(\frac{\partial \theta_e}{\partial y}\right)^2\right] \Big/ \left|\nabla_h \theta_e\right| \tag{5}$$

$$F3 = \left(\frac{\partial \theta_e}{\partial x}\frac{\partial Q}{\partial x} + \frac{\partial \theta_e}{\partial y}\frac{\partial Q}{\partial y}\right) \Big/ \left|\nabla_h \theta_e\right| \tag{6}$$

$$F4 = -\left(\frac{\partial \theta_e}{\partial x}\frac{\partial \omega}{\partial x} + \frac{\partial \theta_e}{\partial y}\frac{\partial \omega}{\partial y}\right)\frac{\partial \theta_e}{\partial z} \Big/ \left|\nabla_h \theta_e\right| \tag{7}$$

$$A = \frac{\partial u}{\partial x} + \frac{\partial v}{\partial y} \tag{8}$$

$$B = \frac{\partial u}{\partial x} - \frac{\partial v}{\partial y} \tag{9}$$

$$C = \frac{\partial v}{\partial x} + \frac{\partial u}{\partial y} \tag{10}$$

where $\nabla_h$is horizontal Hamilton operator, θ_e is equivalent potential temperature, Q is diabatic heating, u, v, and ω are wind velocity along zonal, meridional, and vertical directions, respectively. The frontogenesis function F contains four terms: *F1* is the horizontal divergence term, *F2* is the horizontal deformation term, *F3* is the diabatic heating term, and *F4* is the vertical motion term. Frontogenesis occurs if F is larger than zero. Since the variability of vertical motion ω is quite small along the horizontal direction, *F4* is not included in the calculation.

2.3. The Retrieval of Rain Size Distribution Parameters

Rain size distribution (RSD) parameters can be retrieved from polarimetric variables based on the constrained-gamma (C-G) model proposed by Zhang et al. (2001). A three-parameter gamma function is widely applied to characterize the observed RSDs with the form:

$$N\left(D\right) = N_0 D^{\mu} exp\left(-\Lambda D\right) \tag{11}$$

where D is the particle diameter, N_0 is the intercept parameter, μ is the shape parameter, and Λ is the slope parameter. Previous studies found that the three parameters (N_0, μ, and Λ) in Equation 11 are not independent of each other (Testud et al., 2001; Ulbrich, 1983). A significant positive correlation exists between μ and Λ (Zhang et al., 2001, 2003). Therefore, the C-G model is alternatively established by using the $\mu - \Lambda$ relationship in Equation 11 to reduce the number of independent parameters from three to two. The empirical $\mu - \Lambda$ relationship relies on RSD observations, so it varies among different geographical locations and precipitation types. Based on two-year RSD data collected by four disdrometers located at Guangdong Province, Liu, Wan, et al. (2018) applied a localized $\mu - \Lambda$ relationship ($\Lambda = 0.0241\mu^2 + 0.867\mu + 2.453$) into the C-G model and derived the fitting formula between the RSD parameters (N_0, Λ) and the Guangzhou polarimetric radar data (Z_H, Z_{DR}). The Guangzhou radar (GZRD) is one of the 10 radars used in the present study. Given that these 10 radars are operated in the same scanning mode and the same frequency, and meanwhile they are located in the same limited geographic region, it is probably reasonable to apply the same fitting formula for the merged data from the 10 radars. Therefore, we adopt the same formulas as in Section 3 of Liu, Wan, et al. (2018) to retrieve the RSD parameters. Microphysical variables such as raindrop mass-weighted mean diameter (D_m) and normalized intercept parameter (N_w) can be further calculated by moments of the gamma RSD.

2.4. The Estimation of Liquid and Ice Water Content

Following previous studies (e.g., Carey & Rutledge, 2000; Cifelli et al., 2002; Chang et al., 2015), LWC (M_w) and ice water content (IWC) (M_i) are estimated with the consideration of three scenarios: pure ice, pure rain, and the mixture of ice and rain. The difference reflectivity (Z_{DP}; dB) method (Golestani et al., 1989) is utilized to discriminate the total radar reflectivity (i.e., the horizontal reflectivity Z_H for dual-polarization radars) for ice (Z^{ice}; dBZ) and rain (Z^{rain}; dBZ). Z_{DP} is calculated as follows:

$$Z_{DP} = 10\log\left(Z_H - Z_V\right) \tag{12}$$

where Z_H and Z_V are the horizontal and vertical radar reflectivity in the unit of $mm^6\ m^{-3}$. Z^{rain} is estimated by the localized $Z^{rain} - Z_{DP}$ relationship derived from two-year disdrometer data in Guangdong Province (Li et al., 2019) as follows:

$$Z^{rain} = 0.0044 \times Z_{DP}^2 + 0.58054 \times Z_{DP} + 16.591 \tag{13}$$

and Z^{ice} is thus calculated as follows:

$$Z^{ice} = Z_H - Z^{rain}. \tag{14}$$

If the Z_{DP} method indicates the presence of mix-phase precipitation, then the following Z-M relationship is applied to estimate M_w and M_i (Carey & Rutledge, 2000; Cifelli et al., 2002; Chang et al., 2015; Li et al., 2019):

$$M_w = 3.44 \times 10^{-3} \left(Z_L^{rain}\right)^{4/7} \tag{15}$$

and

$$M_i = 1000\pi\rho_i N_i^{3/7} \left(\frac{5.28 \times 10^{-18} Z_L^{ice}}{720}\right)^{4/7} \tag{16}$$

where Z_L^{rain} (mm^6 m^{-3}) and Z_L^{ice} (mm^6 m^{-3}) is the linear form of Z^{rain} and Z^{ice}, ρ_i (0.917 kg m^{-3}) is the ice density and N_i (4×10^6 m^{-4}) is the intercept parameter of an assumed inverse exponential ice size distribution. M_w is calculated by Equation 15 with $Z_L^{rain} = Z_{HL}$ for pure rain regions while M_i is calculated by Equation 16 with $Z_L^{ice} = Z_{HL}$ for pure ice regions, where Z_{HL} is the observed horizontal radar reflectivity in the unit of mm^6 m^{-3}.

2.5. Dual-Doppler Wind Field Retrieval

The dual-Doppler wind field retrieval is conducted to show the dynamical differences between the two types of convection in the present event. Radial velocity observations from two selected radars are incorporated into the algorithm to retrieve the vertical velocity by the variational adjustment of the anelastic mass continuity equation. Lianzhou radar (LZRD) and Shaoguan radar (SGRD) are selected to retrieve vertical velocity for the frontal convection when it was near the front. GZRD and Shenzhen radar (SZRD) are selected to retrieve vertical velocity for the coexisting frontal convection and warm-sector convection around the coastal region. An additional retrieval domain using the GZRD and SZRD is adopted to include more samples for the comparison. The dual-Doppler retrieval domains are shown by the dashed orange boxes in Figure 1. The wind field retrieval is performed on a Cartesian grid covering 200 km × 200 km × 20 km in meridional, zonal, and vertical directions. The horizontal and vertical resolutions of the retrieval data are 1 and 0.5 km, respectively. A detailed description of the wind field retrieval methodology used herein can be found in Section 2 of Liu, Luo, et al. (2018).

3. Case Description and Environmental Conditions

On June 12–13, 2019, a heavy rainfall event occurred in South China and exhibited the precipitation pattern featured by two coexisting rainbands, namely, an inland frontal rainband and a coastal warm-sector rainband. Figure 2 shows the spatial distribution of IMERG hourly precipitation from 1300 UTC June 12, 2019 to 0200 UTC June 13, 2019 around Guangdong Province (marked by black outlines). Because of the frictional contrast between land and sea, frontogenesis occurred around the coast of South China due to the convergence of wind speed. For the inland region of interest, the frontogenesis was generated by the confluence of warm air from the south and cold air from the north (purple contour in Figure 2), which is identified as a surface cold front. During 1300–1600 UTC June 12, the inland rainband was very close to the surface cold front and it can be regarded as the typical FR (Figures 2a and 2b). In the following four hours, the FR began to move southeastward and vacated from the cold front (Figure 2c). At 2200 UTC June 12, the FR continued to move toward the coastline while new convection was initialized and organized at the coastal area and moved along the coastline (Figures 2d and 2e). Based on the location of the objectively identified front, the coastal organized rainband at later times was located greater than 200 km ahead of the front and in the warm sector, which is regarded as the typical WR. Finally, the frontal convection merged with the

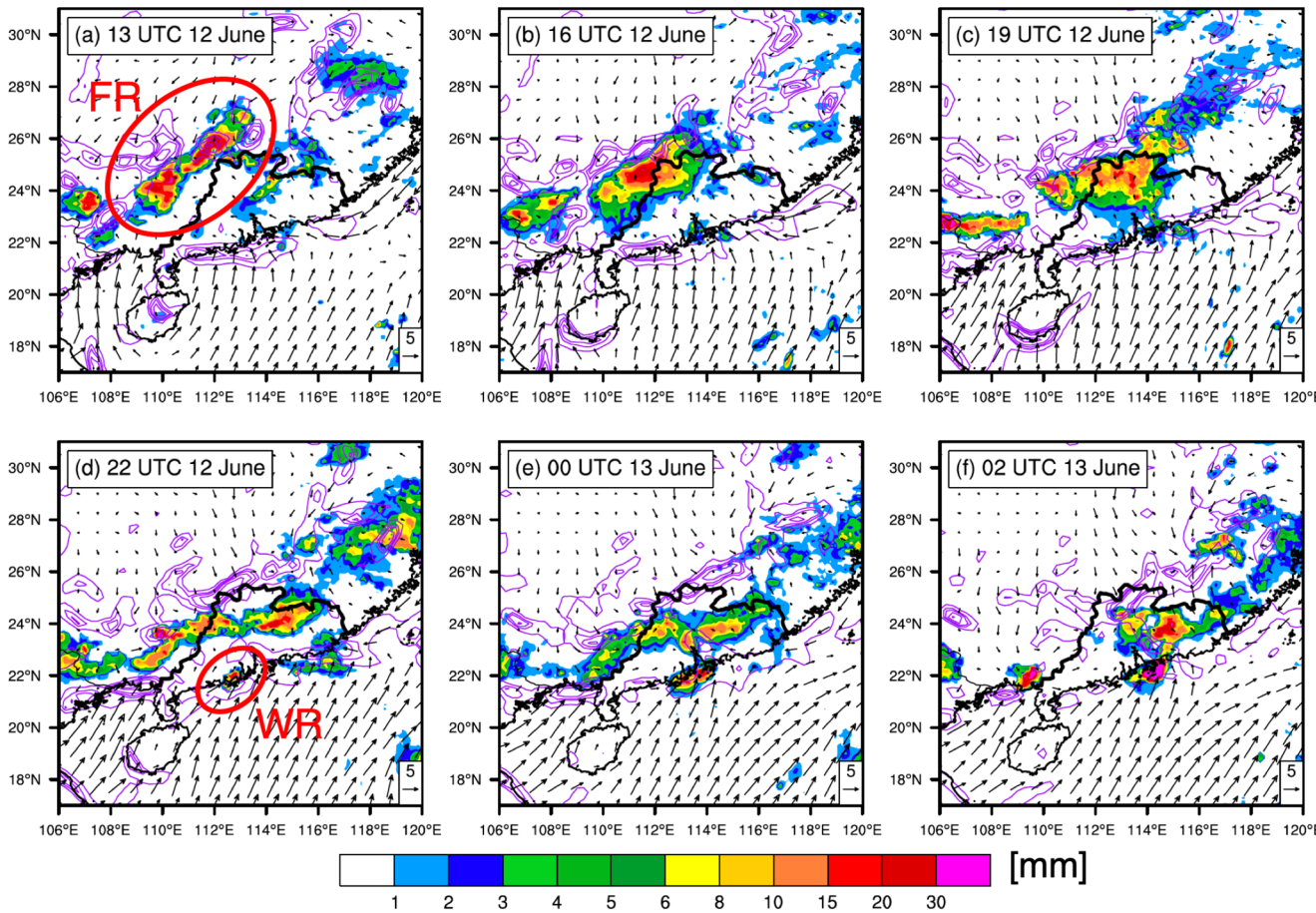

Figure 2. The GPM IMERG hourly precipitation (color filled; mm) and frontogenesis function (purple contours; every 3×10^{-9} K m^{-1} s^{-1} starting from 2×10^{-9} K m^{-1} s^{-1}) at (a) 1300, (b) 1600, (c) 1900, (d) 2200 UTC June 12, 2019, (e) 0000, and (f) 0200 UTC June 13, 2019. The frontogenesis function is calculated at surface layer data from ERA5 reanalysis data. The wind vector denotes the 10-m wind. The red ellipses in (a) and (d) show the identified frontal heavy rainfall and warm-sector heavy rainfall. Guangdong Province is outlined by thick black lines.

organized coastal warm-sector convection at 0200 UTC June 13 (Figure 2f). The maximum hourly rainfall produced by the frontal and warm-sector convection can both exceed 30 mm (Figure 2).

The vacating process of the frontal convection and the initiation of the warm-sector convection are examined by analyzing the synoptic-scale background (Figure 3). At 1600 UTC June 12, a low-level vortex was located at the entrance of the upper-level jet at 200 hPa, where divergence favored the synoptic-scale upward motion and contributed to the development of the low-level vortex (Figure 3a). The low-level vortex was strengthened at 1800 UTC June 12 (Figure 3b) and thus the airflow at 700 hPa was accelerated in the north of Guangdong Province (Figure 3c). The frontal convection ahead of the front was located near the exit of the boundary layer jet at 950 hPa and synoptic-system-related low-level jet at 700 hPa (Figures 3c and 3d). As a result, convergence existed at low levels in this region (marked by the red ellipse in Figures 3e and 3f). These conditions above probably jointly promoted the rebuilding process of the convection ahead of the front. The double low-level jets also played a significant role in the warm-sector convection initiation (CI) of this event, which is consistent with previous studies (e.g., Du & Chen, 2019, Du, Chen, Han, Mai, et al., 2020). The boundary layer jet at 950 hPa over the Northern South China Sea developed and the core of the jet was closer to the coast at 1800 UTC (Figure 3d). The location of CI (blue plus symbol in Figure 3) was at the downstream and left side of the jet at 950 hPa (i.e., the region of positive vorticity), where the convergence developed (Figures 3d and 3f). Besides, the location of CI was located near the entrance of the jet at 700 hPa, where the divergence occurred (Figures 3c and 3e). Compared to the environmental conditions at 1200 UTC, such low-level convergence and middle-to-low level divergence jointly promoted the mesoscale lifting around the location for the warm-sector CI at 1800 UTC (Figures 4a and 4b). In addition to

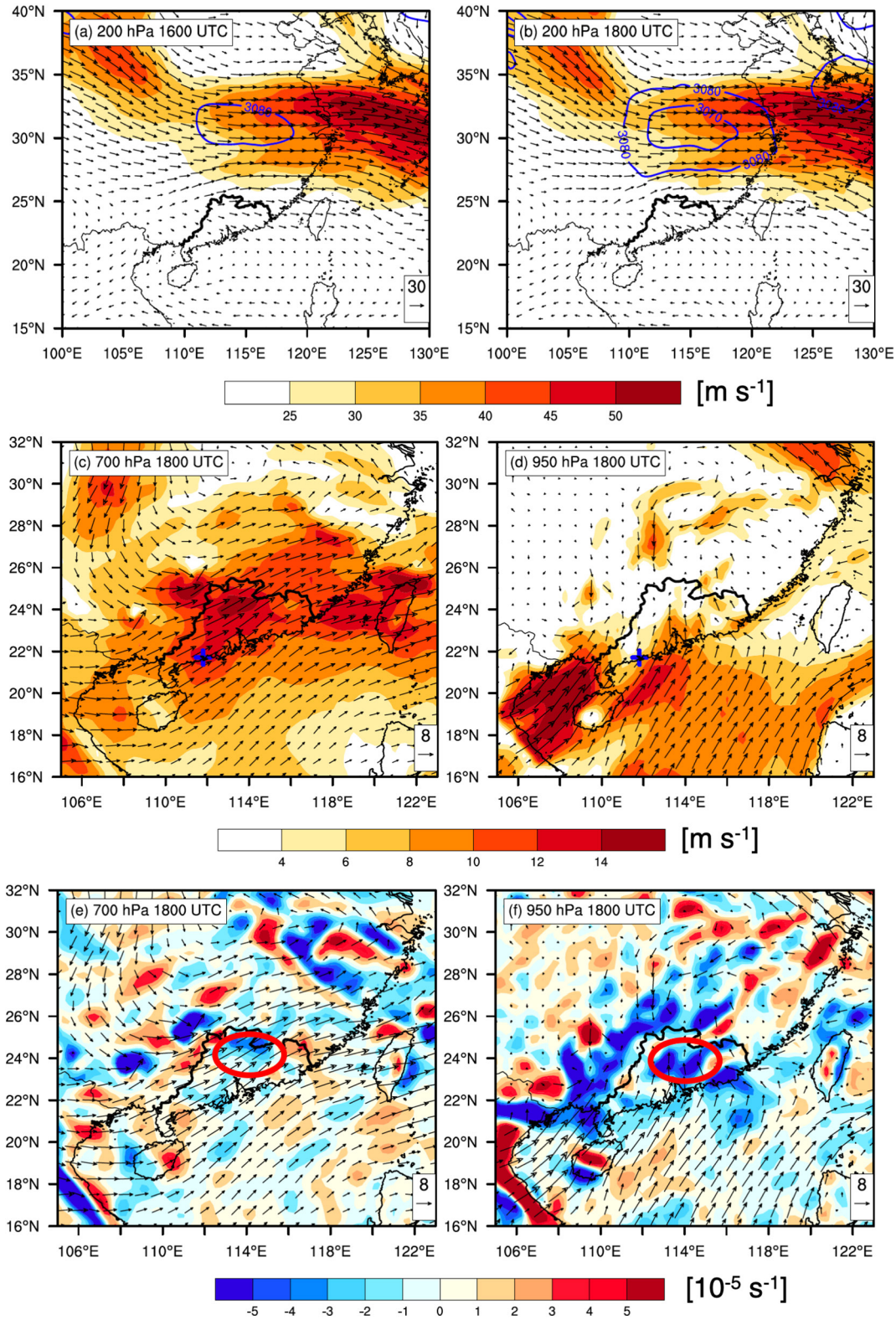

Figure 3. Horizontal distributions of (a)–(d) wind speed (color filled; unit: m/s) and (e) and (f) divergence (color filled; unit: 10^{-5} s^{-1}) at (a), (b) 200 hPa, (c) and (e) 750 hPa, and (d) and (f) 950 hPa from ERA5 reanalysis data. (a) Is at 1600 UTC and (b)–(f) is at 1800 UTC June 12, 2019. The blue contours superimposed in (a) and (b) are the 700-hPa geopotential height (the interval is 10 gpm). The blue plus symbols in (c) and (d) denote the location of the warm-sector convection initiation. The red ellipses in (e) and (f) denote the region that the frontal convection was out ahead of the front.

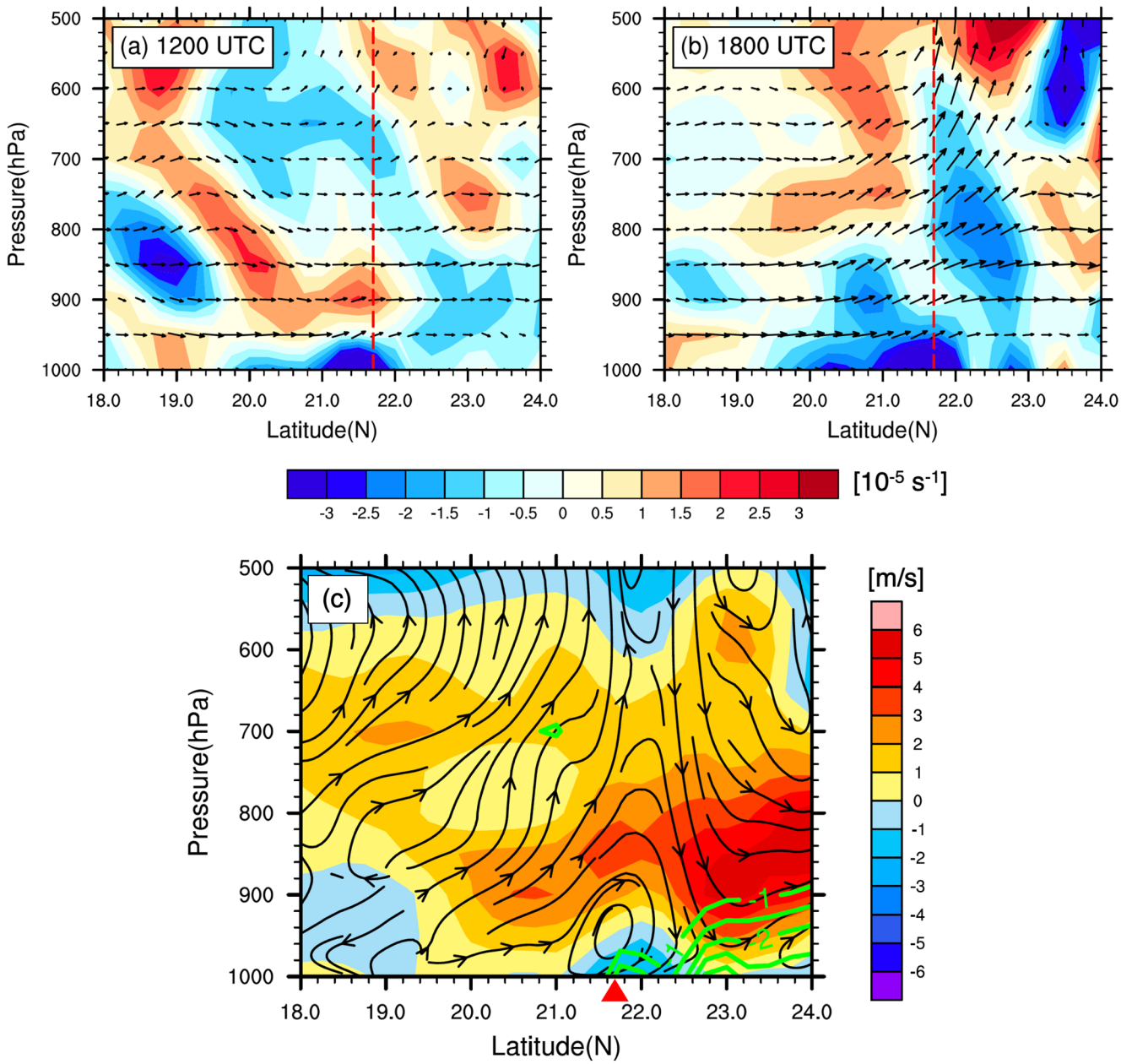

Figure 4. Meridional vertical cross sections of divergence (color filled; unit: 10^{-5} s^{-1}) and wind vectors (vertical velocity multiplied by 100) along 111.75°E (nearest longitude to the blue plus symbol in Figure 3) at (a) 1200 and (b) 1800 UTC June 12, 2019 from ERA5 reanalysis data. (c) Is same as (a) and (b) but for meridional wind differences (color filled; unit: m/s) and temperature differences (green contour; unit: K) between 1800 UTC (0200 LST, i.e., early morning) and 0600 UTC (1400 LST, i.e., afternoon). The red dashed lines in (a) and (b) mark the location of the warm-sector convection initiation. The red triangle in (c) denotes the location of coastline.

the contribution from the low-level jet, the local convergence between the land breeze and southerly winds from the sea additionally provided a favorable condition for the initiation of coastal warm-sector convection (Figure 4c), which is also seen from the climatological study in Wu et al. (2020).

Soundings and wind hodographs from two stations (i.e., Heyuan and Hong Kong) east of the frontal convection and warm-sector convection are further provided in Figure 5. Since the Heyuan sounding was likely to be launched into the frontal rainband at 0000 UTC June 13, we use the Heyuan sounding six hours earlier when the sounding was not into the precipitation. Both the Heyuan and Hong Kong soundings show a very moist layer below 850 hPa and a relatively dry layer between 700 and 500 hPa, suggesting the unstable

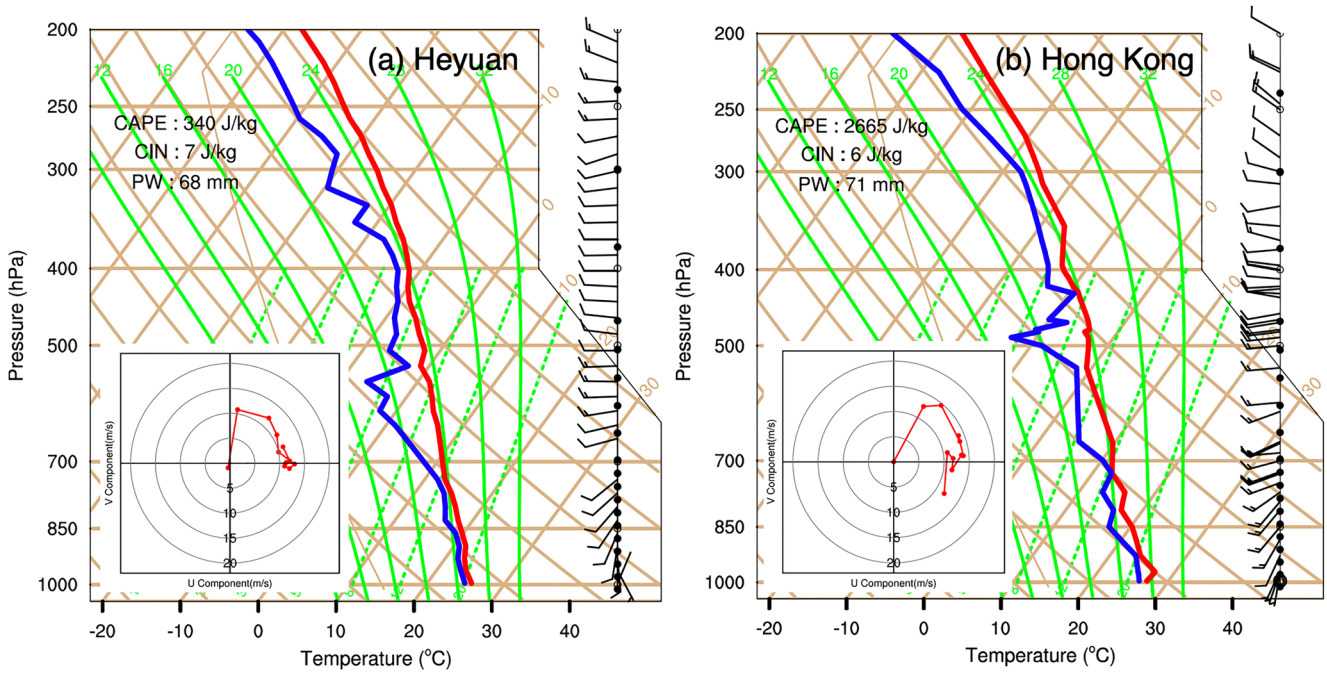

Figure 5. Skew T-logP diagrams at (a) the Heyuan sounding site at 1800 UTC June 12, 2019 and (b) the Hong Kong sounding site at 0000 UTC June 13, 2019. The inserted figures are hodographs for interpolated wind speed from the surface to 10 km height with a 1-km height interval shown by red dots.

atmospheric stratification. The lifting condensation levels are similar for both soundings, but the level of free convection calculated from the Hong Kong sounding is about 300 m lower than that calculated from the Heyuan sounding. Southwesterly winds were observed up to 500 hPa accompanied by the clockwise change in wind direction and the magnitude of 0–3-km bulk vertical wind shear reached approximately 12 m s^{-1}. The environmental conditions were favorable for the development of convection. However, much larger mixed-layer convective available potential energy (CAPE) calculated from the Hong Kong sounding indicates that the coastal warm-sector convection might have a greater potential to develop into deep convection.

4. Microphysical Characteristics of the Frontal and Warm-Sector Convective Cells

4.1. Composite Radar Reflectivity and Identification of Convective Cells

Figure 6 shows the spatial distribution of composite radar reflectivity merged from the ten dual-polarization radars located in South China. In this event, both the frontal convection and warm-sector convection were well observed by those radars. More detailed features can be captured compared to the IMERG precipitation data. For instance, before the frontal convection was rebuilt in the warm sector ahead of the front, the merge processes between the frontal convection and scattered convections from the coast can be observed (Figure 6c). The analysis period starts at 1300 UTC June 12 when the frontal convection began to organize near the surface front and ends at 0200 UTC June 13 when the frontal and warm-sector convections merged together (Figure 6). To compare the microphysical characteristics of the coexisting frontal and warm-sector convections, we use two boxes for sampling. One is fixed at the coastal region (red box B in Figure 6) and the other one is set following the movement of frontal convection (red box A in Figure 6).

In this study, we focus on the convection regions, which were the main contributor to the heavy rainfall. Following Wang et al. (2019), the convective cells (CCs) are identified based on the depth of radar reflectivity. If the points with radar reflectivity larger than 40 dBZ exceed one-third of the total points in each vertical column of gridded data, this column is considered as a CC. The large coverage of 10 radars provides us enough samples at lower levels for robust analysis. Nevertheless, the lack of samples due to nine elevations

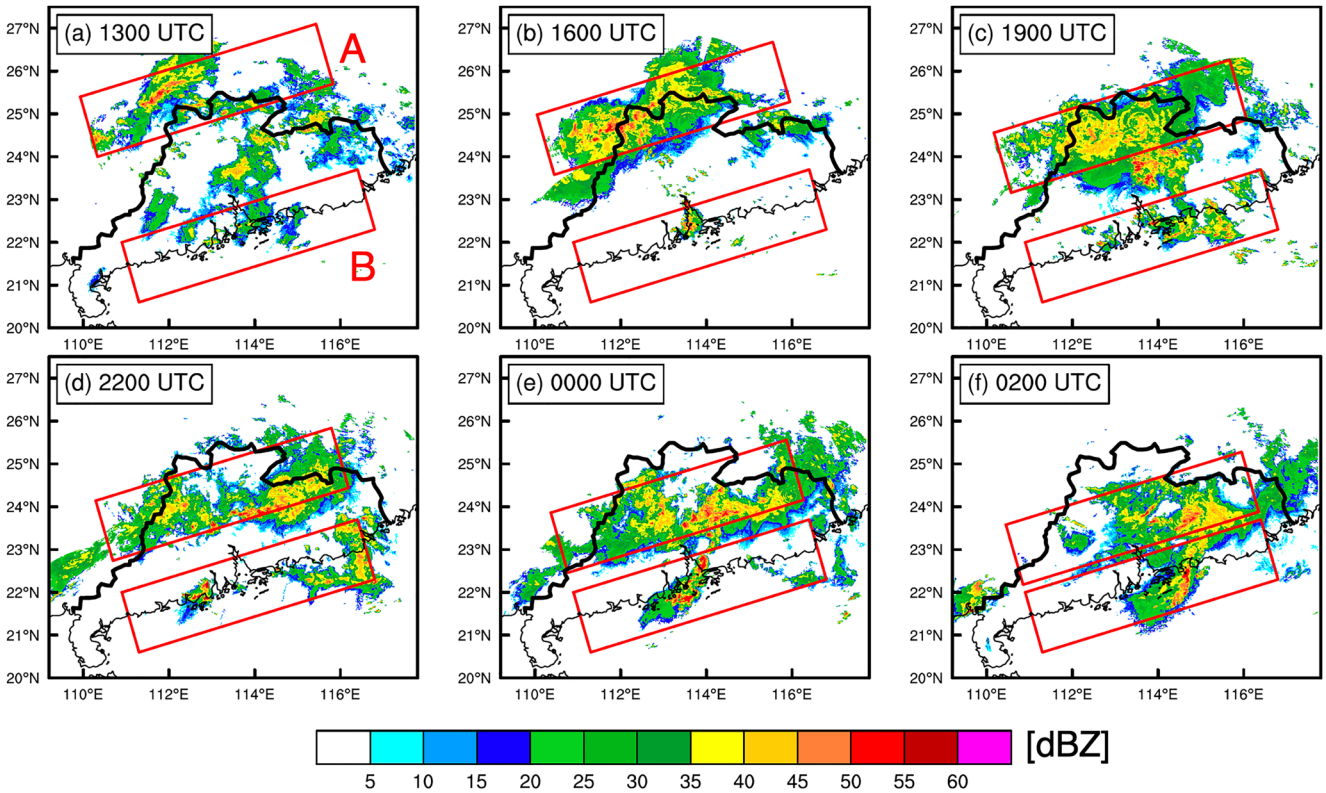

Figure 6. The horizontal distribution of composite radar reflectivity (unit: dBZ) at (a) 1300, (b) 1600, (c) 1900, (d) 2200 UTC June 12, 2019, (e) 0000, and (f) 0200 UTC June 13, 2019. Red boxes denote the analysis domains for the frontal convection (box A) and warm-sector convection (box B).

of operational radar prevents us to conduct robust analysis below 1 km height. Therefore, we only use radar data above 1.0-km altitude (above sea level) for quantitative analysis. Although rain microphysics below 1-km height would not change significantly because of the relatively large environmental humidity, the caveat should be noted since the cold pool near the surface might still affect the raindrop size by evaporation.

4.2. Polarimetric Measurements

Figure 7 shows the contoured frequency by altitude diagrams (CFADs) and the percentile profiles of Z_H, Z_{DR}, and K_{DP} in all the identified frontal and warm-sector CCs during the 13-hr analysis period. The differences in the CFADs of these polarimetric measurements between the warm-sector CCs and frontal CCs are additionally shown in Figures 7g–7i. The height of the freezing level is estimated by the consideration of the correlation coefficient ρ_{hv} and sounding data, which is about 5.3 km for both the CCs. Some negative values of Z_{DR} and K_{DP} above the 0°C level in the CFADs might be partly associated with observational random errors.

The majority of Z_H (defined as frequency larger than 5%) are generally distributed between 40 and 52 dBZ below the freezing level in both the frontal and warm-sector CCs (cf. Figures 7a and 7d). However, above the freezing level, the decrease of Z_H with height varies between the frontal and warm-sector CCs. At 12-km altitude, most Z_H decreases to 8–22 dBZ for the frontal CCs (Figure 7a) while most Z_H declines to 10–32 dBZ for the warm-sector CCs (Figure 7d). The differences in CFADs of Z_H between these two types of CCs clearly show that the warm-sector CCs have more large values than the frontal CCs (Figure 7g). This is also validated by differences in the profiles of Z_H at the 50th, 90th, and 99th percentiles between these two types of CCs (Figure 7j). The vertical profile of radar reflectivity is commonly used as an indicator for storm intensity in previous studies (e.g., Xu et al., 2009; Zipser & Lutz, 1994; Zipser et al., 2006). Larger vertical profiles of Z_H at all the three percentiles indicate that the warm-sector CCs generally have a stronger convection intensity than the frontal CCs in this event.

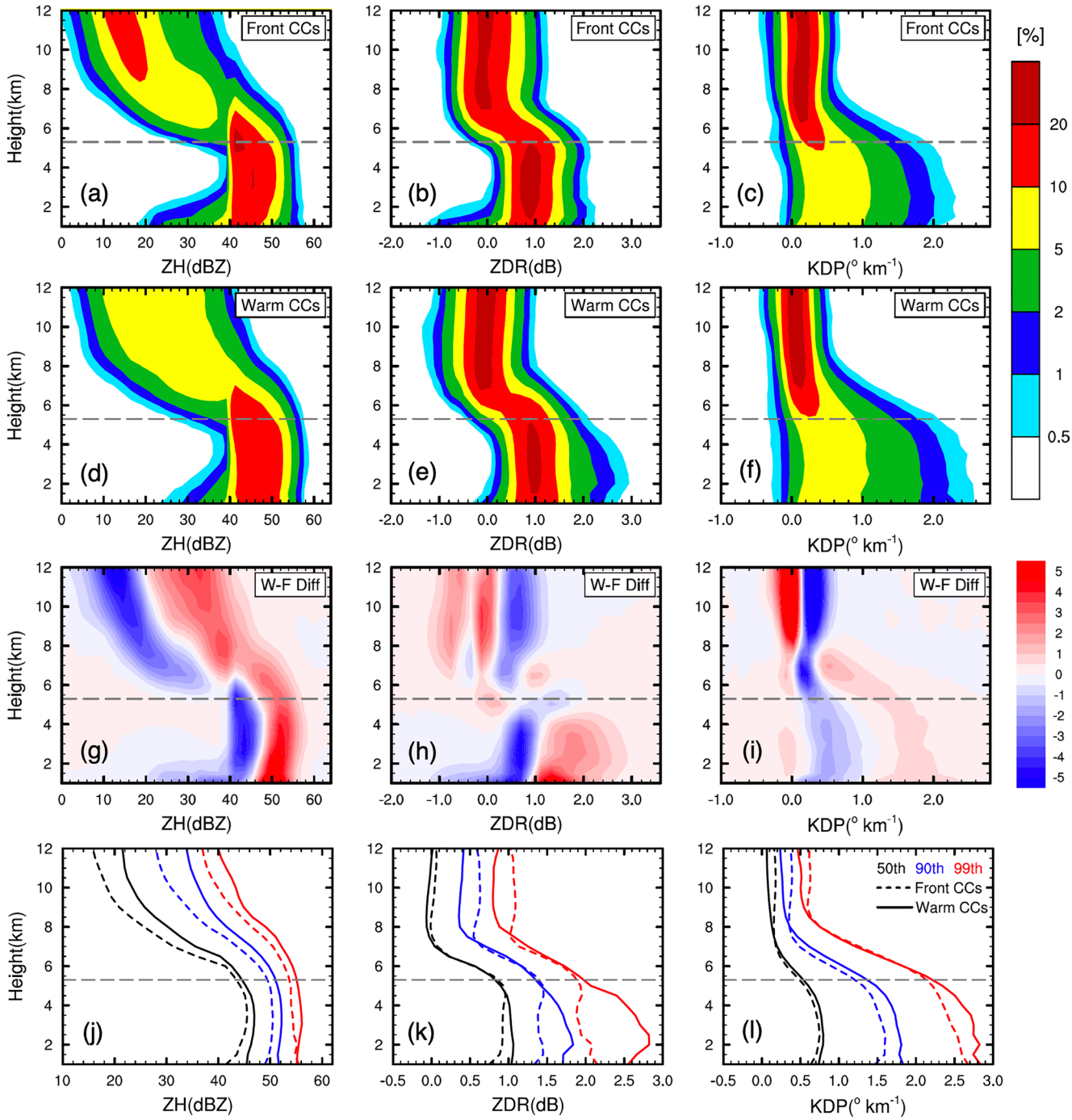

Figure 7. The CFADs (unit: %) of (a) Z_H, (b) Z_{DR}, and (c) K_{DP} for the frontal CCs. (d)–(f) Are the same as (a)–(c) but for the warm-sector CCs. (g)–(i) Are the CFADs difference between the warm-sector CCs and frontal CCs. (j–l) Are the 50th, 90th, and 99th percentile profiles of Z_H, Z_{DR}, and K_{DP} for the frontal CCs (dashed lines) and warm-sector CCs (solid lines). The analysis period is from 1300 UTC June 12, 2019 to 0200 UTC June 13, 2019. The height of the melting level is indicated by dashed gray lines.

From 12 to 7 km height, the distribution of most Z_{DR} samples in the frontal and warm-sector CCs is centered nearly zero with more positive values in the frontal CCs (Figures 7b and 7e). A prominent downward increase of Z_{DR} is seen from 7-km altitude to the freezing level. Below the freezing level, a part of the frequency contours of Z_{DR} in the warm-sector CCs show a faster increase toward the lower altitude while those in the frontal CCs generally remain constant (cf. Figures 7b and 7e). As a result, the warm-sector CCs show

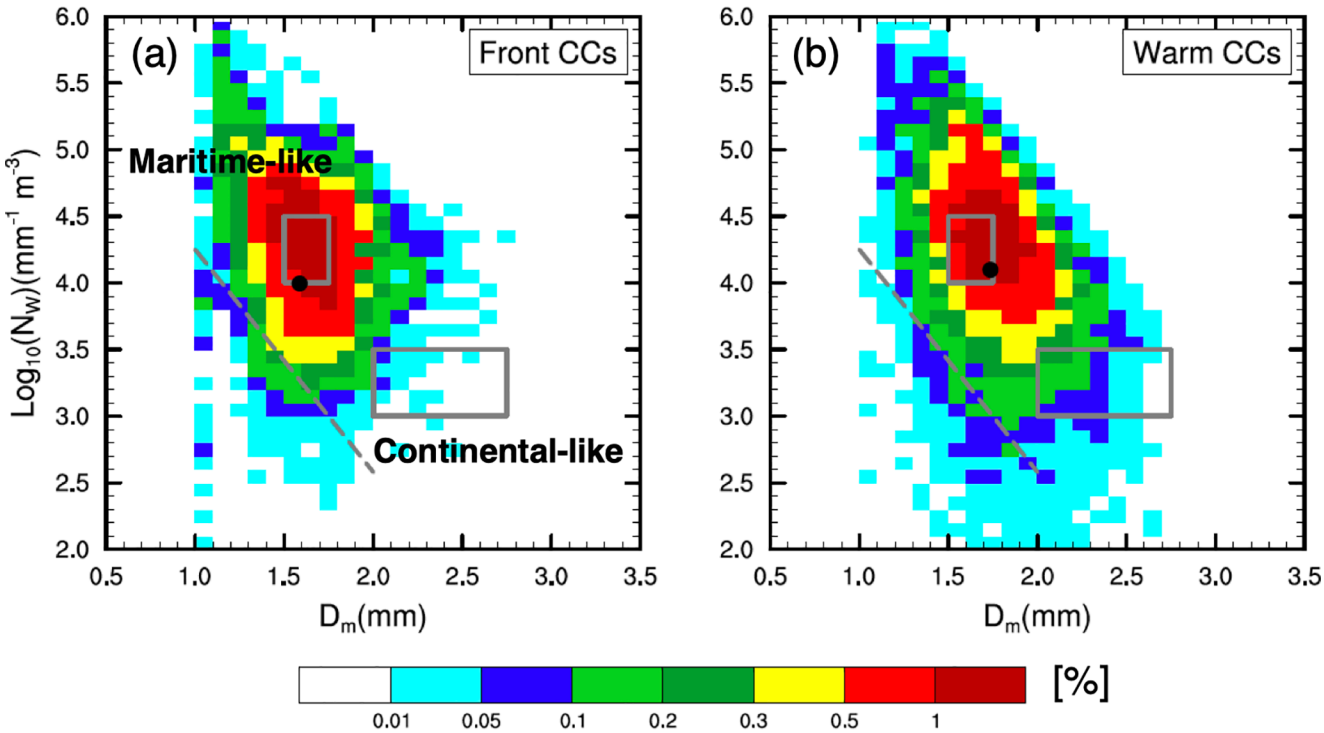

Figure 8. The joint PDFs (unit: %) of D_m and $\log_{10}(N_w)$ at 1-km altitude for (a) frontal CCs and (b) warm-sector CCs. The analysis period is from 1300 UTC June 12 to 0200 UTC June 13, 2019. The gray dashed line denotes the fitting line for stratiform precipitation while two gray rectangles represent the maritime and continental convective clusters in $D_m - \log_{10}(N_w)$ space from Bringi et al. (2003). The black dots in (a) and (b) show the locations of mean values of D_m and $\log_{10}(N_w)$.

a larger frequency for Z_{DR} larger than 1 dB below 4 km height (Figure 7h). A more obvious discrepancy in Z_{DR} between the warm-sector and frontal CCs can also be found in the 90th and 99th percentile profiles (Figure 7k). The maximum differences in Z_{DR} at the 90th and 99th percentile profiles below 5 km altitude are around 0.4 and 0.7 dB, respectively. Higher Z_{DR} below the melting level suggests that the raindrop size is larger in the warm-sector CCs.

The distributions of K_{DP} for both CCs are slightly different above 7-km altitude (cf. Figures 7c and 7f). However, the K_{DP} of warm-sector CCs is distributed more broadly toward values larger than 1.5° km^{-1} below the melting level (Figure 7i), resulting in approximately 0.3° km^{-1} higher at 90th and 99th percentile profiles (Figure 7l). The result indicates higher rainwater content in the warm-sector CCs.

Overall, the differences in Z_H and K_{DP} between the two types of CCs below the melting level at 90th and 99th percentile profiles are relatively small compared to those in Z_{DR} (Figures 7j–l). Since Z_H and K_{DP} are related to both particle diameter and number concentration while Z_{DR} is only closely associated with particle oblateness (or diameter), the greater difference in Z_{DR} between the two types of CCs but with relatively similar Z_H or K_{DP} implies a considerable number of larger raindrops in the warm-sector CCs.

4.3. Rain Microphysics

To directly reveal the microphysical characteristics of raindrops for the two types of CCs, the RSD parameters are retrieved by Z_H and Z_{DR} based on the C-G model as described in Section 2c. Figure 8 shows the joint probability distribution functions (PDFs) between the mass-weighted mean diameter D_m and the logarithmic scale of normalized intercept parameter $\log_{10}(N_w)$ at 1.0-km altitude (i.e., the lowest height with samples for robust analysis). The gray dashed line in Figure 8 denotes an empirical fitting line for stratiform precipitation in $D_m - \log_{10}(N_w)$ space from Bringi et al. (2003). Samples are almost located on the right side of this dashed line, which indicates the convective rain type. The joint PDFs for both CCs are mainly confined within the area bounded by D_m with a range of 1.5–2.0 mm and $\log_{10}(N_w)$ with a range of 3.5–5.0 mm^{-1}

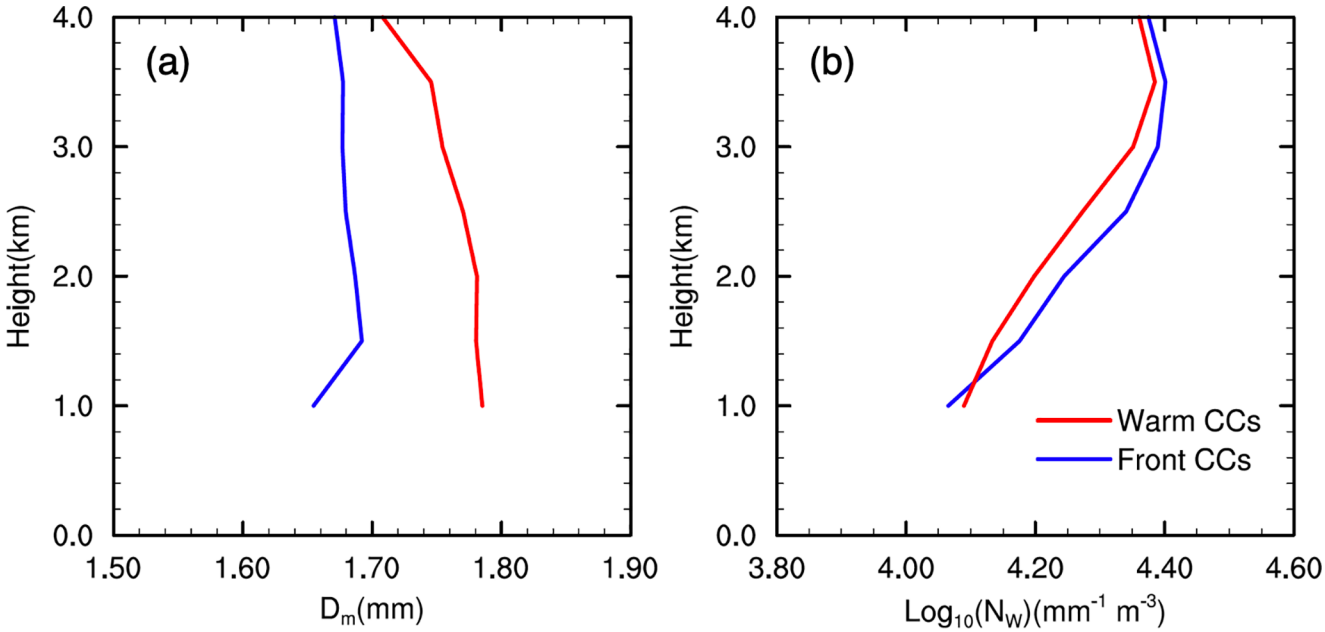

Figure 9. Mean profiles of the retrieved (a) D_m (unit: mm) and (b) $\log_{10}(N_w)$ (unit: mm^{-1} m^{-3}) averaged over the frontal CCs (blue lines) and warm-sector CCs (red lines). The analysis period is from 1300 UTC June 12, 2019 to 0200 UTC June 13, 2019.

m^{-3}. The mean D_m and $\log_{10}(N_w)$ of the warm-sector CCs are about 0.15 mm and 0.1 mm^{-1} m^{-3} higher than those of the frontal CCs. The mean values of both CCs are still within the "maritime-like" cluster where the RSDs are characterized by a high number concentration of small raindrops. Since these two precipitation systems were generally coexisting in the same climatic region, it is not surprising that they present similar raindrop characteristics in an average sense. However, RSDs of the warm-sector CCs also partly have a "continental-like" characteristic with some samples featured by a considerable number concentration of large raindrops. By contrast, very few RSDs in the frontal CCs are within the "continental-like" cluster.

The vertical distribution of D_m and $\log_{10}(N_w)$ averaged over the two types of CCs are further compared in Figure 9. For the frontal CCs, retrieved D_m shows a slight increase from 4 to 1.5 km height and a decrease from 1.5 to 1 km height. The decrease of D_m from 1.5 to 1 km height might be caused by the lack of samples since the frontal convection was located in a relatively high-terrain region at most times (cf. Figures 1 and 6). In the warm-sector CCs, retrieved D_m shows an increasing tendency with decreasing height. Besides, the two types of CCs both show a decrease of $\log_{10}(N_w)$ from 4 km height to 1 km height. The increase of D_m and decrease of $\log_{10}(N_w)$ with decreasing height in the two types of CCs are probably resulted from the interactions among collision, coalescence, and evaporation (Dolan et al., 2013; Wen et al., 2017). However, the warm-sector CCs generally have a more efficient increase of raindrop size than the frontal CCs.

Since both the frontal and warm-sector convections have mixed-phase processes in this event, initial raindrops partly come from the melting of rimed ice particles and thus these raindrops usually have relatively large sizes. Both types of convection are different from shallow convection, in which the initial raindrops are primarily produced by the collision between cloud droplets condensed from water vapor. In general, the warm-sector CCs have stronger convective updrafts (see Section 5) to lift more liquid droplets above the freezing level and thus probably promote the riming process. Large raindrops melted from more rimed ice particles in the warm-sector CCs experience further growth in raindrop size by a more efficient collision–coalescence process below the melting level (i.e., collection of cloud droplets). In this study, we mainly regard the more efficient collection of cloud droplets as more active warm rain processes to explain the differences in raindrop size between the frontal and warm-sector CCs.

Caveats should be noted since Bringi et al. (2003) did not use the same method to retrieve D_m and $\log_{10}(N_w)$ as in this study, and the values of retrieved D_m and $\log_{10}(N_w)$ and relevant fitting line in Figure 8 are somewhat sensitive to the $\mu-\Lambda$ relationship. These factors could influence the interpretation of the RSDs

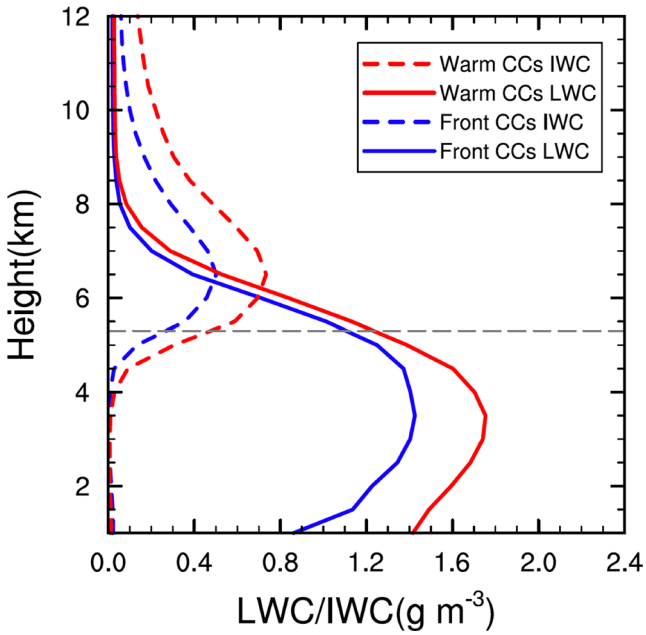

Figure 10. The vertical profiles of LWC (solid lines; unit: g m^{-3}) and IWC (dashed lines; unit: g m^{-3}) averaged over the frontal CCs (blue lines) and warm-sector CCs (red lines). The analysis period is from 1300 UTC June 12, 2019 to 0200 UTC June 13, 2019. The height of the melting level is indicated by a dashed gray line.

characteristics to a certain degree (i.e., maritime-like or continental-like) but the absolute difference in RSDs between the frontal and warm-sector CCs would not be altered.

4.4. LWC and IWC

Mean vertical profiles of LWC and IWC for the two types of CCs are also examined using the Z_{DP} method (see Section 2d) as shown in Figure 10. The warm-sector CCs produce more IWCs than the frontal CCs, which might be resulted from more active ice-related processes caused by the stronger updrafts. Below the melting level, larger LWC is also seen in the warm-sector CCs, which is consistent with larger K_{DP} in the warm-sector CCs shown in Figure 7. The difference in the maximum of IWC for the two types of CCs is about 0.25 g m^{-3} while the corresponding difference in LWC is about 0.4 g m^{-3}. This suggests that the production of more IWCs can only partly contribute to the discrepancy in LWC while the warm rain processes can also play a role in the LWC differences between the two types of CCs.

4.5. Temporal Evolution of Microphysical Characteristics for the Frontal CCs

In the last three subsections, microphysical characteristics of the frontal and warm-sector CCs are compared quantitatively. However, unlike the warm-sector convection, the frontal convection in this event experienced an evident temporal evolution from the first stage near the front (stage 1) to the second stage that merged with scattered convections from the coast (stage 2), and then to the third stage that rebuilt ahead of the front (stage 3). Stage 1 is a typical frontal convection period while the latter two stages are somewhat not as typical as stage 1. Here we further compare the microphysical features during the three stages of the frontal CCs. Figure 11 shows the time-height distributions of Z_H, Z_{DR}, and K_{DP} averaged over the frontal CCs along with the corresponding mean profiles of these polarimetric variables averaged over the three stages. There are pronounced differences among the three stages of the frontal CCs. Z_H undergoes an evolution from the strongest period to the relatively weak period but then it gets enhanced again at stage 3 (Figures 11a). The convection intensity at stage 3 is similar to that at stage 1 below 4 km height, but it is obviously weaker than stage 1 above 4 km height (Figures 11d). The change of Z_{DR} generally shows a consistent increase above the melting level (Figure 11b). Below the melting level, Z_{DR} experiences an increase at stage 1 following a temporary decrease during 1700–1900 UTC and then increases again at stage 3 (Figure 11b). Compared to stage 1, the mean Z_{DR} is even larger at stage 3 (Figure 11e). For all three stages, the values of K_{DP} increase remarkably from 8-km height to lower levels (Figure 11c). K_{DP} is largest at stage 1 while the change of K_{DP} is relatively small for the latter two stages. The difference in the mean profiles between stages 2 and 3 only exists below 3 km height (Figure 11f).

We further compare the microphysical features of raindrops for stages 1 and 3 when organized frontal convection was observed. Stage 3 has comparable or even slightly larger Z_H than stage 1 below the melting level (Figure 11d). Meanwhile, low-level Z_{DR} averaged during stage 3 is about 0.2 dB greater than that in stage 1 but the corresponding mean K_{DP} is much smaller (Figures 11e and 11f). It suggests a large number of small raindrops at stage 1 of the frontal CCs. In contrast, stage 3 might produce relatively large raindrops but with less number concentration, which is somewhat similar to the rain microphysics of the warm-sector CCs.

The vertical distribution of hydrometeors at stages 1 and 3 is compared in Figure 12. The frontal CCs at stage 1 have more rimed graupel particles, which is associated with the larger convection intensity at stage 1. The mixture of rain and hail can still account for approximately 5% frequency at 2 km height while the corresponding frequency is only 2% for stage 3 (cf. Figures 12a and 12b), which suggests a more profound riming process at stage 1. However, the occurrence frequency of heavy rain at stage 3 is greater than that at

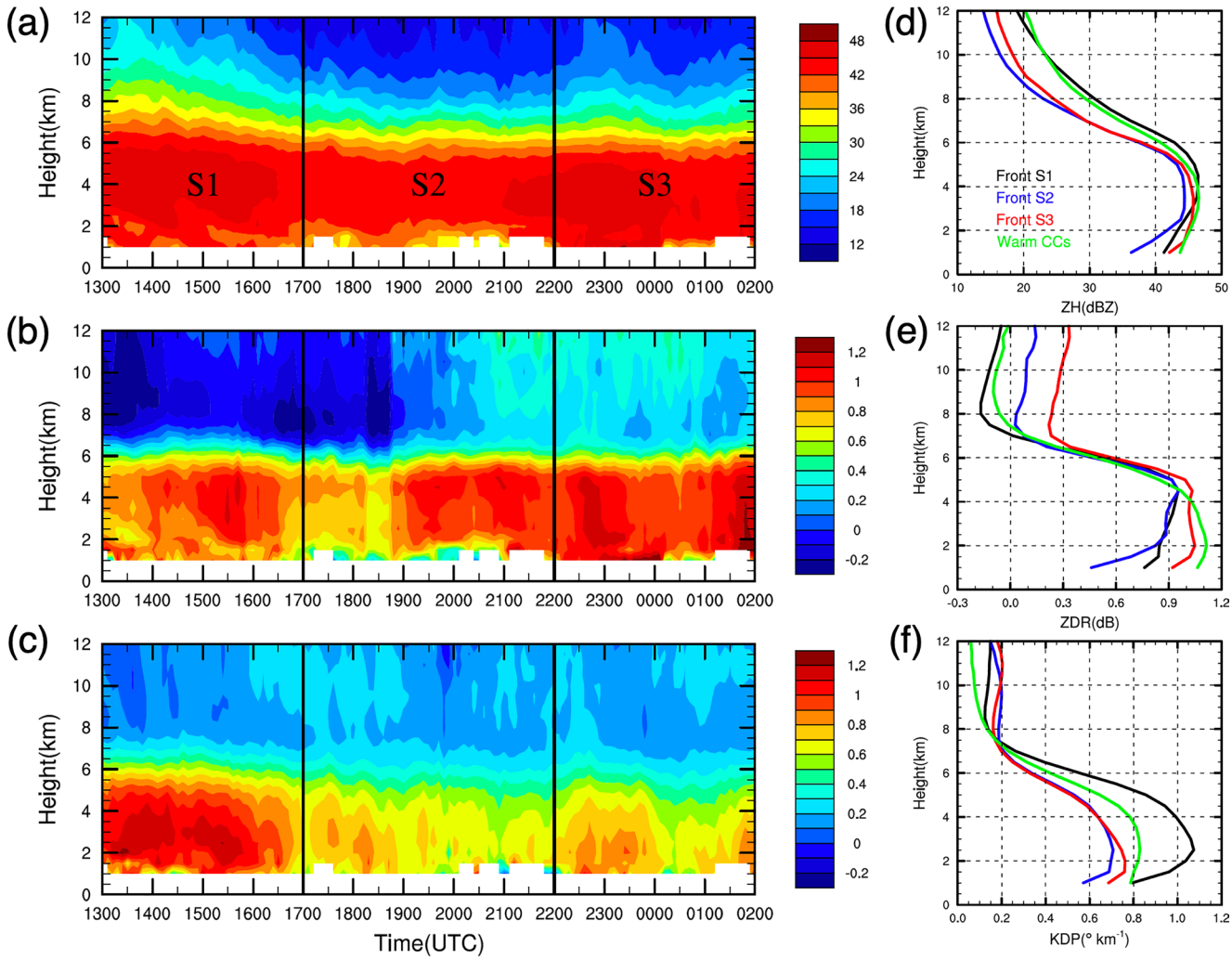

Figure 11. The time-height distributions of (a) Z_H, (b) Z_{DR}, and (c) K_{DP} averaged over the frontal CCs. (d)–(f) Are the mean profiles of Z_H, Z_{DR}, and K_{DP} averaged over the warm-sector CCs and three stages of the frontal CCs. The black lines in (a)–(c) mark the time to separate the three stages for the frontal CCs.

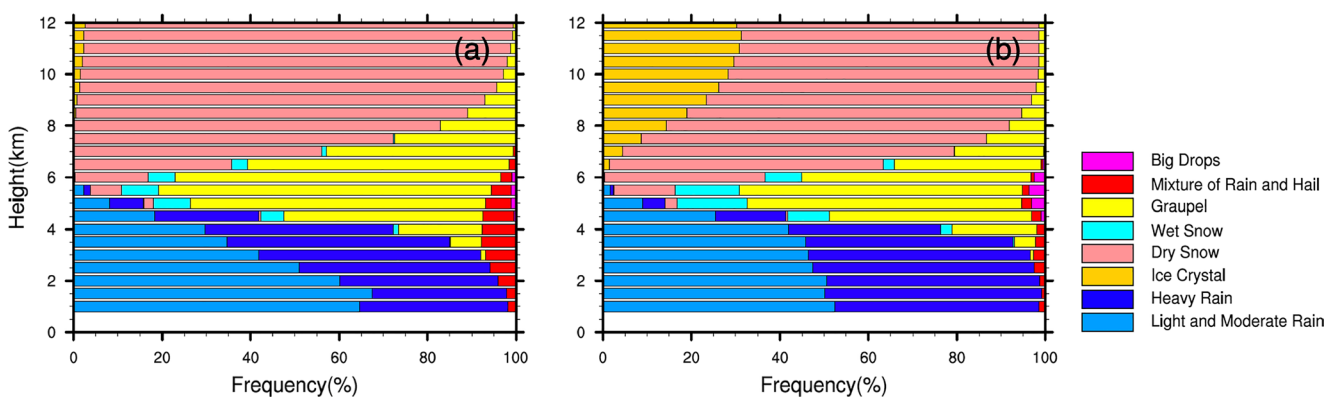

Figure 12. The stacked frequency (unit: %) of each identified hydrometeor by altitude for the frontal CCs at (a) stage 1 and (b) stage 3. The meanings of each color for identified hydrometeors are listed in the legend.

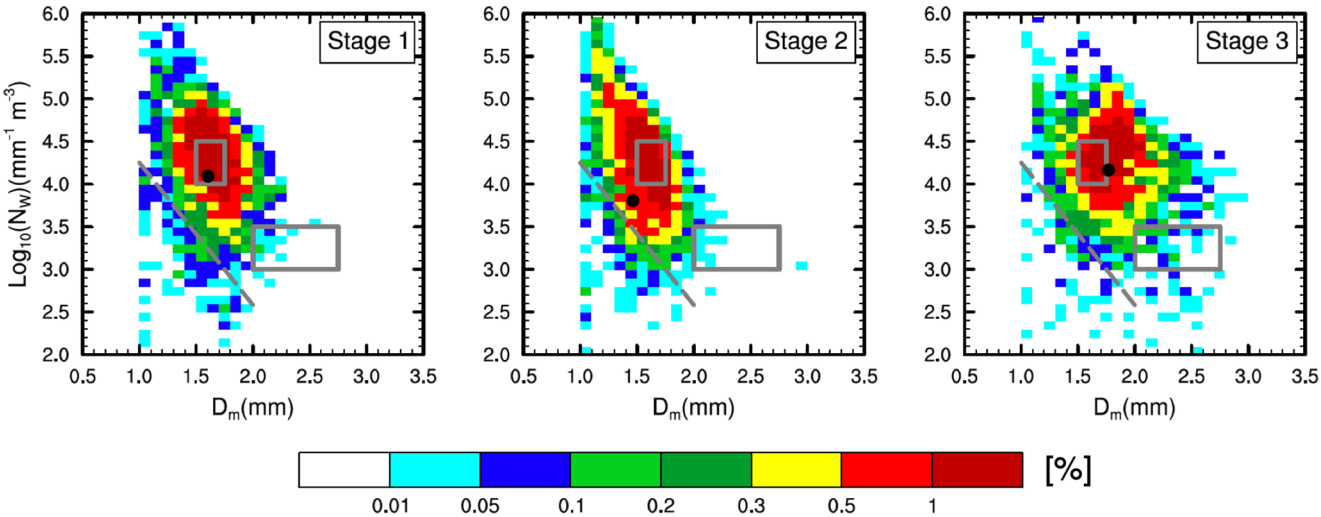

Figure 13. Same as Figure 8, except for the joint PDFs (unit: %) of D_m and $\log_{10}(N_w)$ at 1-km altitude at three stages of the frontal CCs.

stage 1 because of larger Z_{DR} (i.e., larger raindrop) at stage 3, which is easier to be categorized as heavy rain by the HCA.

4.6. Comparison Between the Warm-Sector CCs and the Frontal CCs at Different Stages

To compare the polarimetric features between the warm-sector CCs and the frontal CCs at different stages, the mean profiles of Z_H, Z_{DR}, and K_{DP} averaged over the warm-sector CCs are also shown in Figures 11d–11f (green lines). The mean profile of Z_H for the frontal CCs at stage 1 is quite similar to that of the warm-sector CCs except that the latter shows a larger Z_H below 4 km height. A similar large Z_H below 4 km height is found for the warm-sector CCs and the frontal CCs at stage 3 while their difference in Z_H is prominent above 4 km height (Figure 11d). All the three stages of frontal CCs show smaller Z_{DR} than the warm-sector CCs below 4 km height, although the low-level Z_{DR} at stage 3 is the largest (Figure 11e). Below the melting level, the mean K_{DP} of the warm-sector CCs is smaller than that of the frontal CCs at stage 1 but larger than that at stage 2 and 3 (Figure 11f).

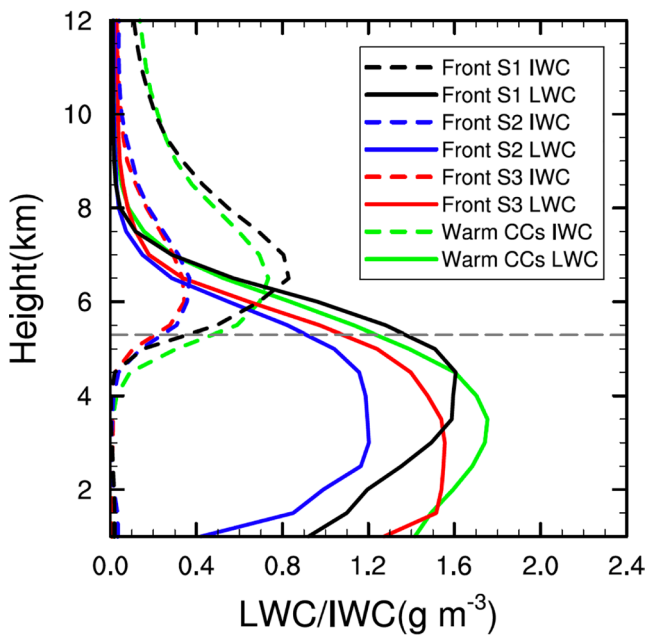

Figure 14. Same as Figure 10, except for the mean profiles of LWC (solid lines; unit: g m^{-3}) and IWC (dashed lines; unit: g m^{-3}) for the frontal CCs at three stages and the warm-sector CCs.

The joint PDFs of D_m and $\log_{10}N_w$ for the frontal CCs at different stages are shown in Figure 13. The pattern of joint PDFs of D_m and $\log_{10}N_w$ for the frontal CCs is mainly contributed by the first two stages (cf. Figures 8 and 13). For the frontal CCs at stage 3, its pattern is somewhat close to that of the warm-sector CCs, showing more samples with large D_m and small $\log_{10}N_w$ than the first two stages.

Vertical profiles of retrieved LWCs and IWCs are further compared in Figure 14. The differences between the frontal CCs at different stages and the warm-sector CCs are similar to those in the mean profiles of Z_H. It is because the retrievals of LWC and IWC are highly determined by the values of Z_H (see Equations 15 and 16). The mean IWC in the warm-sector CCs is similar to that of the frontal CCs at stage 1 and higher than those at stages 2 and 3, suggesting active ice-based processes in the frontal CCs at stage 1. However, even with similar IWC, the mean LWC in the warm-sector CCs is about 0.2 g m^{-3} larger than that of the frontal CCs at stage 1 below 4-km height. The frontal CCs at stage 3 show the largest LWC among three stages and thus are closest to the warm-sector CCs, indicating that warm rain processes become active at stage 3. It is noted that K_{DP} (depends on LWC) is largest at stage 1 (Figure 11f) but retrieved LWC

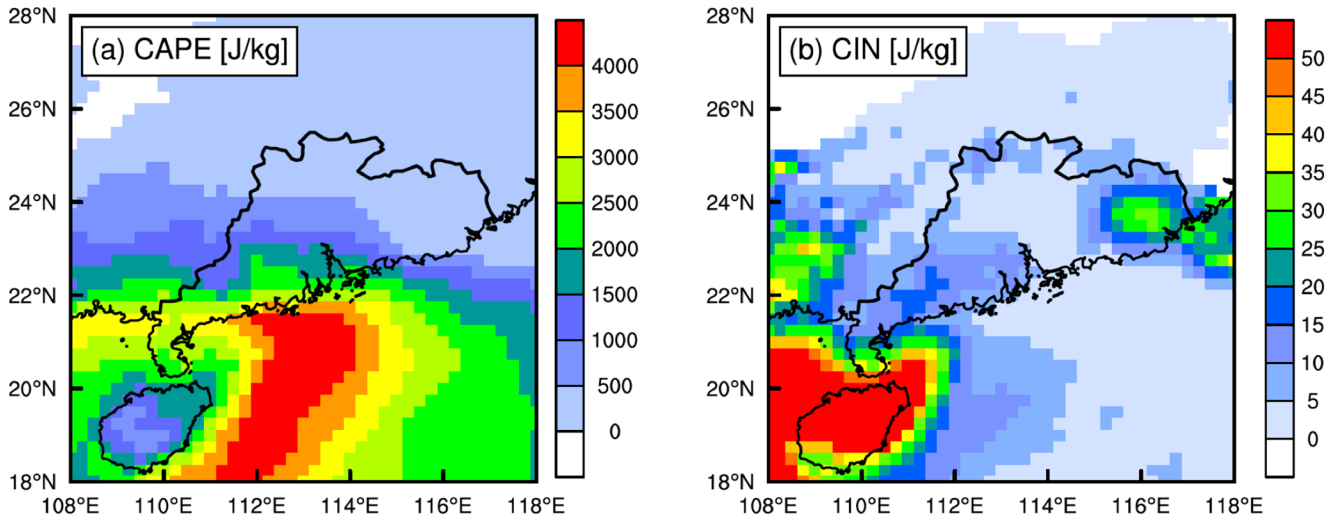

Figure 15. The horizontal distribution of (a) CAPE (unit: J kg^{-1}) and (b) CIN (unit: J kg^{-1}) calculated from ERA5 reanalysis data averaged from 1300 UTC June 12, 2019 to 0200 UTC June 13, 2019.

at stage 1 is not the largest. This is likely because the retrieval algorithm highly depends on Z_H, which is proportional to the particle number and sixth power of particle diameter. Therefore, the retrieval algorithm used in this study somewhat amplifies the relatively small raindrop size at stage 1, resulting in moderate retrieved LWC.

5. Discussion: Possible Reasons for the Microphysical Differences

Figure 15 shows the spatial distributions of CAPE and convective inhibition (CIN) averaged over the analysis period. Generally, the warm-sector CCs were situated in the coastal region of high CAPE greater than 2000 J kg^{-1} while the inland frontal CCs were supplied by the CAPE smaller than 1000 J kg^{-1}. The environmental CIN for both CCs was relatively weak. The difference in CAPE suggests that the environmental condition favors the development of warm-sector CCs. When accompanied by other favorable conditions, the warm sector could have a larger possibility to grow into deeper convection than the frontal CCs.

To validate the differences in convection intensity and better understand the microphysical differences, the dual-doppler wind field retrieval is conducted for this case. The radar reflectivity observations merged from 10 radars are regridded onto the grid of each wind field retrieval so that the identified CCs can be matched with the retrieved vertical velocity. The comparison is limited to the identified CCs with vertical velocity (w) greater than 1 m s^{-1} to focus on the convective updrafts. The analysis period for the frontal convection at stage 1 is from 1400 UTC to 1600 UTC June 12, 2019 while the analysis period for the frontal convection at stage 3 and the warm-sector convection is from 2300 UTC June 12, 2019 to 0100 UTC June 12, 2019. Figure 16 shows the vertical profiles of convective updrafts at the 50th, 99th, and 99th percentiles. Compared to the frontal CCs at stage 3, larger w is found at stage 1, which is consistent with more identified graupel particles above the 0 °C level during the typical frontal convection period (Figure 12). More importantly, the warm-sector CCs generally have a larger w than the frontal CCs at these three percentiles, suggesting that a more favorable condition to lift the cloud droplets above the freezing level and thus to promote the riming process. A more active riming process can produce more rimed ice particles for melting. Therefore, there might be more initial large raindrops in the warm-sector CCs, which could experience a further increase in size by a more efficient collection of cloud water when they fall toward lower levels. This can partly explain the discrepancy in quantitative results of raindrop microphysics between the frontal and warm-sector CCs (Figure 8).

For the frontal CCs near the front (i.e., stage 1), they can also develop into deep convection without abundant CAPE but by strong dynamical forcing of front lifting, which is evidenced by the large w at the 99th

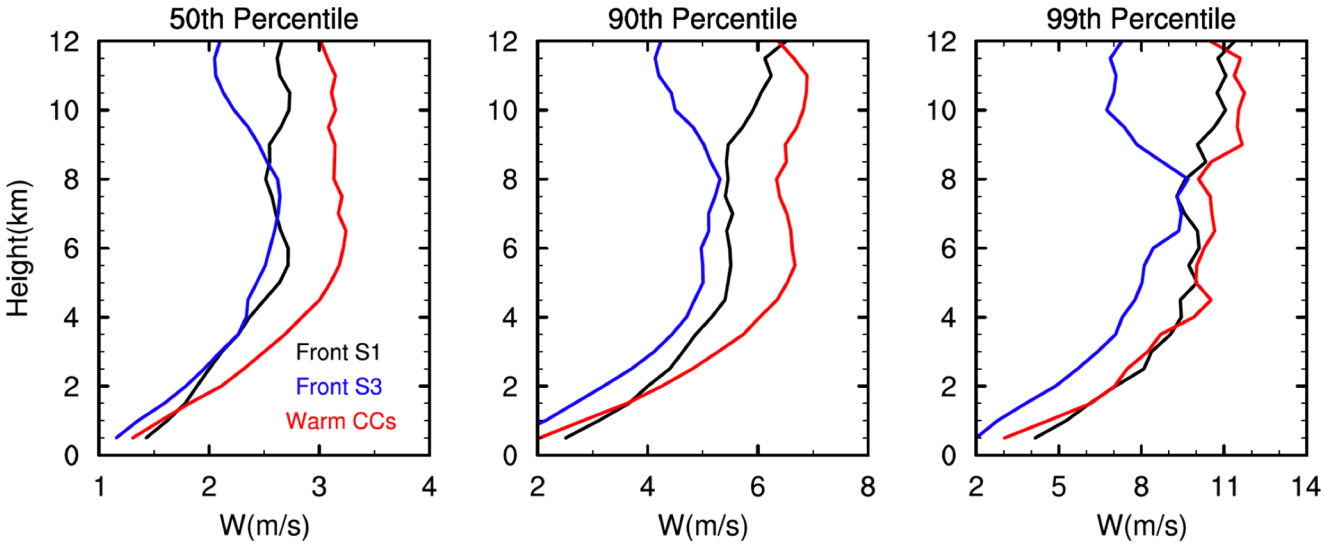

Figure 16. Vertical profiles of convective updrafts at the 50th, 99th, and 99th percentiles. The black lines denote the frontal CCs at stage 1, the blue lines denote the frontal CCs at stage 3, and the red lines denote the warm-sector CCs.

percentile (Figure 16). However, the warm-sector CCs still produce larger raindrops than the frontal CCs near the front. Therefore, their difference in raindrop size cannot be explained only by the convection intensity.

Recent studies have shown that low-level rotation in the storms can enhance precipitation through dynamical effects and potentially increase the warm rain processes (e.g., Nielsen & Schumacher, 2018, 2020). Radial velocity from the GZRD and LZRD are thus used to show the rotation features when the strongest convection occurred. From Figure 17 (black contour denotes the identified convective cells), we can see that the rotation features exist in both the frontal and warm-sector convection. When the frontal convection was near the front, the rotation mainly occurred at the east part of the frontal system (Figures 17a–17c). When it was away from the front and gradually moved into the warm sector, the frontal convection was established by the convergence of wind speed (inland convection region in Figures 17d–17f). As for the warm-sector convection, the rotation feature in the convection region is obvious, especially for those over the sea (coastal region in Figures 17d–17f). Large values (>2 dB) of Z_{DR} were also observed by the GZRD in these convective cells over the sea. It is possible that the low-level rotation additionally accelerates the growth of raindrop size by enhancing the warm rain processes (e.g., the collision-coalescence process between cloud droplets and raindrops) for the warm-sector convection. Although the frontal convection at stage 1 (Figures 17a–17c) also had the rotation feature, it only obviously existed in the eastern part. For the warm-sector convection, the rotation feature dominated most of the convection region, which can affect more samples of convective cells. This might result in a larger mean raindrop size in the warm-sector CCs than that in the frontal CCs at either stage 1 or stage 3.

Besides, the low-level water vapor mixing ratio at the coastal region was larger than that in the inland region (Figure 18), which could further contribute to more active warm rain processes by potentially providing more cloud droplets to be collected by raindrops. It might result in an even larger mean raindrop size in the warm-sector CCs (Figure 11e). The frontal convection rebuilt in the warm sector was close to the coastal area of a larger low-level water vapor mixing ratio (Figure 18b). Due to the similar promoted warm rain processes, the raindrop size of the frontal CCs at stage 3 was increased compared to those at stage 1 (Figure 11e).

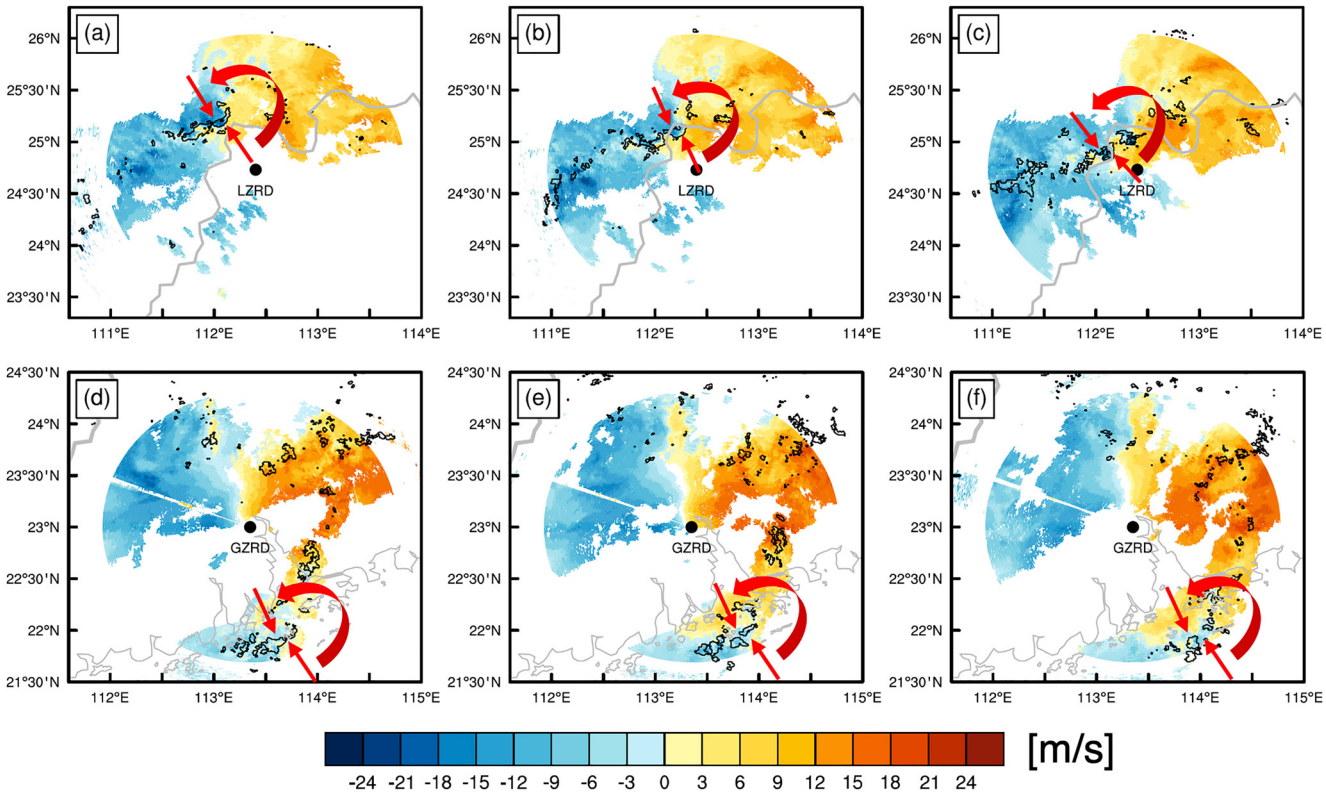

Figure 17. Spatial distribution of radial velocity at the 2.4° elevation observed by Lianzhou radar (LZRD) at (a) 1400, (b) 1430, and (c) 1500 UTC June 12, 2019. (d)–(f) Are same as (a)–(c) but for Guangzhou radar (GZRD) at (d) 0000, (e) 0030, and (f) 0100 UTC June 13, 2019. Black contours denote the identified convective cells. The locations of LZRD and GZRD are marked by the black dots. Red arrows mark the radial wind direction toward and away from the radars.

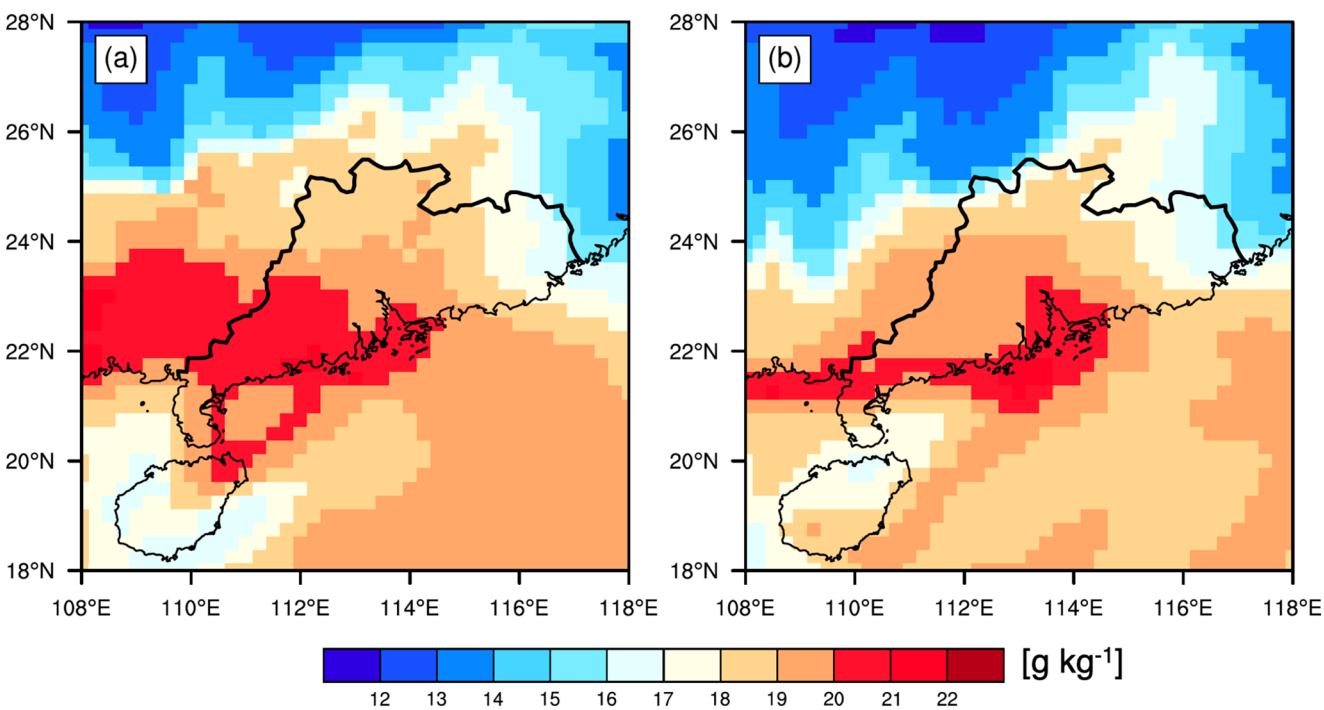

Figure 18. Spatial distribution of mean water vapor mixing ratio (unit: g kg^{-1}) between 900 and 1,000 hPa layers averaged during (a) 1400–1500 UTC June 12, 2019 and (b) 0000–0100 UTC June 13, 2019.

6. Summary

In the present study, we use polarimetric observations merged from 10 radars as well as IMERG precipitation, ERA5 reanalysis, and sounding data to investigate a heavy rainfall event that occurred on June 12–13, 2019 in South China. The purposes are to identify the differences in microphysical characteristics of the coexisting frontal and warm-sector convection, and also to investigate the possible influence of dynamical and thermodynamical conditions on their microphysical differences.

In this event, the inland frontal convection at first occurred near the front forced by the dynamical lifting of the front but it was later vacated from the front and rebuilt ahead of the front. The vacating and rebuilding processes were likely associated with the convergence of wind speed at the exit of a boundary layer jet. Meanwhile, the coastal organized warm-sector convection was initialized by the low-level convergence and middle-to-low level divergence related to the double low-level jets in South China. In addition, the local convergence between the nocturnal land breeze and southerly low-level flows from the sea possibly further promoted the initiation of the warm-sector convection.

By comparing the polarimetric measurements of the frontal and warm-sector convection, we examine the microphysical differences between the two types of convection. For all the identified CCs during the 13-hr period, the warm-sector CCs generally have larger Z_H than the frontal CCs, suggesting a stronger convection intensity. Below the melting level, the warm-sector CCs show greater Z_{DR} and K_{DP}, indicating a larger raindrop size and higher LWC. Compared to the frontal CCs, retrieved RSDs at 1 km height further reveal that the warm-sector CCs partly have a "continental-like" feature with more large raindrops, which is consistent with much larger Z_{DR} in 90th and 99th percentile profiles.

More large raindrops might be attributed to the melting of more rimed ice particles due to more active ice-based microphysical processes in deep convection. An unstable environment over the sea or coastal area during the East Asia monsoon season provides abundant CAPE from the ocean for the development of warm-sector convection. Combined with other local forcings, the warm-sector convection has a larger possibility to develop significantly with prominent ice-based processes (especially riming process) than the frontal convection in most circumstances. The stronger warm-sector convection is further evidenced by the larger convective updraft velocities derived from the dual-Doppler radar retrieval. This can largely explain the discrepancy in the quantitative comparison of raindrop microphysics between the frontal and warm-sector CCs.

Interestingly, the warm-sector CCs still manifest larger raindrops than the frontal CCs when their convective intensity is similar. The temporal evolution of microphysical properties in the frontal convection is significant. The frontal convection can be also quite strong when it was near the front, which was dynamically forced by the front lifting (stage 1). Compared to the later stage when it was organized again ahead of the front (stage 3), the frontal convection near the front had more active ice-based microphysical processes with more rimed ice particles aloft. However, the raindrop size of frontal CCs near the front was smaller than that of the frontal CCs ahead of the front.

There are some possible reasons for the microphysical differences illustrated above. When the frontal convection moved ahead of the front and was closer to the coast, warm rain processes were likely promoted due to the higher low-level humidity around the coastal region, resulting in a larger mean raindrop size at stage 3 than that at stage 1. Apart from the contribution from greater low-level moisture, the low-level rotation might also potentially increase the warm rain processes to a certain degree from the dynamical perspective. The warm-sector convection shows more evident rotation features, especially for those CCs over the sea. By contrast, the frontal convection only partially exhibits the feature of low-level rotation at stage 1 and has no obvious low-level rotation at stage 3. Therefore, the combined effects of low-level moisture and rotation probably lead to a larger mean raindrop size in the warm-sector CCs than that in the frontal CCs at either stage 1 or stage 3. The major findings of the microphysical differences between the warm-sector CCs and frontal CCs at different stages and the possible influence of environmental factors are summarized in a schematic diagram as shown in Figure 19.

The comparison between the frontal CCs at stage 1 and those at stage 3 suggests that large raindrops might not necessarily be related to deep convection with active ice-based processes. Meanwhile, it also indicates

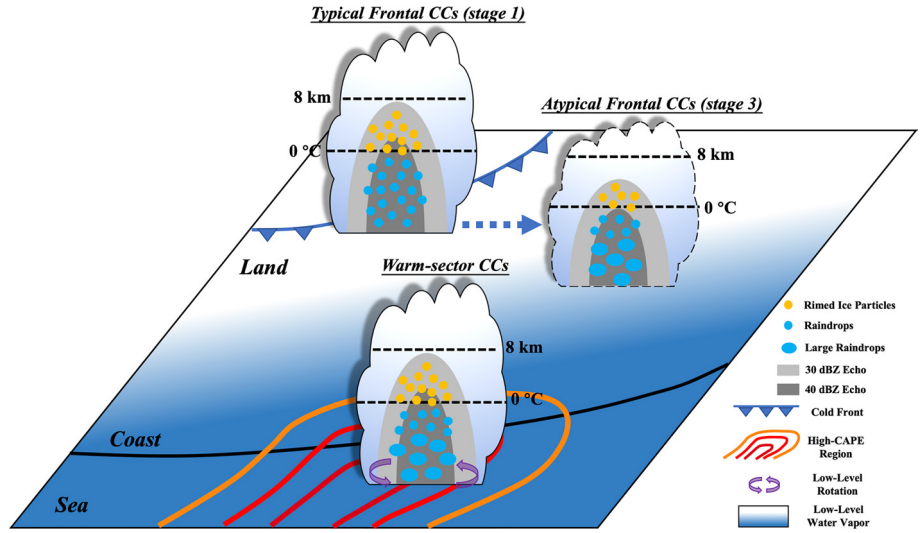

Figure 19. Schematic diagram depicting the microphysical characteristic differences between the warm-sector CCs and frontal CCs at different stages and the possible influence of environmental factors.

that warm rain processes are likely more important in determining the raindrop size for convection with ice-based processes near the coastal area. Processes affecting the raindrop microphysics in this event are somewhat different from those in the typical tropical oceanic and midlatitude continental convections. Tropical oceanic convection is usually shallow convection due to lower vertical velocities (e.g., Houze et al., 2015; Zipser et al., 2006). With abundant moisture, warm rain processes dominate the change of raindrop size. But due to the absence of contribution from the melting of rimed ice particles and the limitation of relative weak updrafts to hold raindrops aloft for a sufficient collision–coalescence process, the mean raindrop size is typically smaller in the oceanic convection (e.g., Bringi et al., 2003; Dolan et al., 2018). Intense deep convection is more commonly observed over land (e.g., Houze et al., 2015; Zipser et al., 2006). Strong vertical velocities can continuously lift small cloud droplets above the freezing level to enhance the ice-based processes for continental deep convection. This can somewhat suppress the warm rain processes, since cloud droplets are lifted above the freezing level by strong updrafts before they experience the collision–coalescence process to form raindrops, especially for the deep convections growing in high cloud condensation nuclei concentrations over land (e.g., Rosenfeld et al., 2008). As a result, the raindrops are mainly melted from heavily rimed particles, and thus the mean raindrop size is typically larger in the continental convection (e.g., Bringi et al., 2003; Dolan et al., 2018). Besides, some small raindrops might be evaporated when falling into the air with a relatively low humidity over inland regions, which could further lead to a larger mean raindrop size and a lower mean raindrop number.

This event occurred around coastal regions, where continental and maritime influences coexist (Lang et al., 2010). Consistent with previous studies focusing on convections at subtropical regions (e.g., Chang et al., 2015; Rowe et al., 2011, 2012; Xu & Zipser, 2015), results in this study show that different meteorological forcings can lead to the variability in the microphysical structure of different types of convections. Moreover, the low-level rotation might be an important factor leading to more large raindrops. The relative importance of the thermodynamical factor (i.e., CAPE, moisture) and dynamical factor (i.e., low-level rotation) might be clarified by conducting numerical simulations but beyond the scope of this study.

The microphysical characteristic differences between the coexisting frontal and warm-sector convection shown in this study are only based on one typical heavy rainfall case. Most of the operational radars in South China just completed the upgrade to dual-polarization mode recently. With more data collection after the upgrade, we plan to include more heavy rainfall cases in South China to obtain the microphysical characteristics of the frontal and warm-sector convection from a perspective of climatology in the future.

Data Availability Statement

The radar data used in this study has been uploaded at http://dx.doi.org/10.17632/cdhndc3cvm.2 on Mendeley. The ERA5 reanalysis data and sounding data can be downloaded at https://cds.climate.copernicus.eu/cdsapp#!/dataset/10.24381/cds.bd0915c6 and http://weather.uwyo.edu/upperair/sounding.html, respectively.

Acknowledgments
The authors thank three anonymous reviewers for their helpful comments to greatly improve the manuscript. This study is supported by the National Key Research and Development Program of China (Grant 2018YFC1507402), the National Natural Science Foundation of China (Grants 42005001, 42122033, 41875055, and 42075006), Guangzhou Science and Technology Plan Projects (202002030346), the Fundamental Research Funds for the Central Universities (19lgzd08), and the Young Elite Scientists Sponsorship Program by CAST (2018QNRC001). We thank the Chinese Academy of Meteorological Sciences for providing radar data and the ECMWF for providing ERA5 reanalysis data.

References

Akiyama, T. (1973). The large-scale aspects of the characteristic features of the Baiu front. *Papers in Meteorology and Geophysics*, *24*, 157–188. https://doi.org/10.2467/mripapers1950.24.2_157

Barnes, H. C., & Houze, R. A., Jr. (2014). Precipitation hydrometeor type relative to the mesoscale airflow in oceanic deep convection of the Madden–Julian oscillation. *Journal of Geophysical Research: Atmospheres*, *119*, 13990–14014. https://doi.org/10.1002/2014jd022241

Bluestein, H. B. (1986). Fronts and Jet Streaks: A Theoretical Perspective. In P. S. Ray (Ed.), *Mesoscale meteorology and forecasting* (pp. 173–215). American Meteorological Society. https://doi.org/10.1007/978-1-935704-20-1_9

Bringi, V. N., & Chandrasekar, V. (2001). *Polarimetric Doppler weather radar: Principles and applications* (p. 636). Cambridge University Press.

Bringi, V. N., Chandrasekar, V., Hubbert, J., Gorgucci, E., Randeu, W. L., & Schoenhuber, M. (2003). Raindrop size distribution in different climatic regimes from disdrometer and dual-polarized radar analysis. *Journal of the Atmospheric Sciences*, *60*, 354–365. https://doi.org/10.1175/1520-0469(2003)060<0354:rsdidc>2.0.co;2

Carey, L., & Rutledge, S. (2000). The relationship between precipitation and lightning in tropical island convection: A C-band polarimetric radar study. *Monthly Weather Review*, *128*, 2687–2710. https://doi.org/10.1175/1520-0493(2000)128<2687:trbpal>2.0.co;2

Chang, W., Lee, W., & Liou, Y. (2015). The kinematic and microphysical characteristics and associated precipitation efficiency of subtropical convection during SoWMEX/TiMREX. *Monthly Weather Review*, *143*, 317–340. https://doi.org/10.1175/mwr-d-14-00081.1

Chen, G., Lan, R., Zeng, W., Pan, H., & Li, W. (2018). Diurnal variations of rainfall in surface and satellite observations at the monsoon coast (South China). *Journal of Climate*, *31*, 1703–1724. https://doi.org/10.1175/jcli-d-17-0373.1

Chen, G., Zhao, K., Wen, L., Wang, M., Huang, H., Wang, M., et al. (2019). Microphysical characteristics of three convective events with intense rainfall observed by polarimetric radar and disdrometer in Eastern China. *Remote Sensing*, *11*. https://doi.org/10.3390/rs11172004

Chen, X., Zhang, F., & Zhao, K. (2016). Diurnal variations of the land–sea breeze and its related precipitation over South China. *Journal of the Atmospheric Sciences*, *73*, 4793–4815. https://doi.org/10.1175/jas-d-16-0106.1

Cifelli, R., Petersen, W. A., Carey, L. D., Rutledge, S. A., & da Silva Dias, M. A. F. (2002). Radar observations of the kinematic, microphysical, and precipitation characteristics of two MCSs in TRMM LBA. *Journal of Geophysical Research*, *107*, 8077. https://doi.org/10.1029/2000jd000264

Ding, Y. (1994). *Monsoons over China* (p. 419). Kluwer Academic.

Dolan, B., Fuchs, B., Rutledge, S. A., Barnes, E. A., & Thompson, E. J. (2018). Primary modes of global drop-size distributions. *Journal of the Atmospheric Sciences*, *75*, 1453–1476. https://doi.org/10.1175/jas-d-17-0242.1

Dolan, B., Rutledge, S. A., Lim, S., Chandrasekar, V., & Thurai, M. (2013). A robust C-band hydrometeor identification algorithm and application to a long-term polarimetric radar dataset. *Journal of Applied Meteorology and Climatology*, *52*, 2162–2186. https://doi.org/10.1175/jamc-d-12-0275.1

Du, Y., Chen, G., Han, B., Bai, L., & Li, M. (2020). Convection initiation and growth at the coast of South China. Part II: Effects of the terrain, coastline and cold pools. *Monthly Weather Review*, *148*, 3871–3892. https://doi.org/10.1175/mwr-d-20-0090.1

Du, Y., Chen, G., Han, B., Mai, C., Bai, L., & Li, M. (2020). Convection initiation and growth at the coast of South China. Part I: Effect of the marine boundary-layer jet. *Monthly Weather Review*, *148*, 3847–3869. https://doi.org/10.1175/mwr-d-20-0089.1

Du, Y., & Chen, G. X. (2018). Heavy rainfall associated with double low-level jets over southern China. Part I: Ensemble-based analysis. *Monthly Weather Review*, *146*, 3827–3844. https://doi.org/10.1175/mwr-d-18-0101.1

Du, Y., & Chen, G. X. (2019). Heavy rainfall associated with double low-level jets over southern China. Part II: Convection initiation. *Monthly Weather Review*, *147*, 543–565. https://doi.org/10.1175/mwr-d-18-0102.1

Golestani, Y., Chandrasekar, V., & Bringi, V. N. (1989). Intercomparison of multiparameter radar measurements. *Preprints, 24th conference on radar meteorology* (pp. 309–314). American Meteorological Society.

Houze, R. A., Jr., Rasmussen, K. L., Zuluaga, M. D., & Brodzik, S. R. (2015). The variable nature of convection in the tropics and subtropics: A legacy of 16 years of the tropical rainfall measuring mission satellite. *Reviews of Geophysics*, *53*, 994–1021. https://doi.org/10.1002/2015rg000488

Huang, S. S. (1986). *Heavy rainfall over southern China in the pre-summer rainy season (in Chinese)* (p. 244). Guangdong Science and Technology Press.

Huffman, G. J., Bolvin, D. T., Nelkin, E. J., & Tan, J. (2019). *Integrated multi-satellite retrievals for GPM (IMERG) technical documentation* (p. 77). NASA Technical Documents. Retrieved from https://pmm.nasa.gov/sites/default/files/document_files/IMERG_doc_190909.pdf

Kumjian, M. R., & Ryzhkov, A. V. (2008). Polarimetric signatures in supercell thunderstorms. *Journal of Applied Meteorology Climatology*, *47*(7), 1940–1961. https://doi.org/10.1175/2007jamc1874.1

Lang, T. J., Rutledge, S. A., & Cifelli, R. (2010). Polarimetric radar observations of convection in northwestern Mexico during the North American Monsoon Experiment. *Journal of Hydrometeorology*, *11*, 1345–1357. https://doi.org/10.1175/2010jhm1247.1

Li, H., Wan, Q., Peng, D., Liu, X., & Xiao, H. (2019). Multiscale analysis of a record-breaking heavy rainfall event in Guangdong, China. *Atmospheric Research*, *232*, 104703.

Li, X., & Du, Y. (2021). Statistical relationships between two types of heavy rainfall and low-level jets in South China. *Journal of Climate*, *34*, 8549–8566. https://doi.org/10.1175/JCLI-D-21-0121.1

Li, Z., Luo, Y., Du, Y., & Chan, J. C. L. (2020). Statistical characteristics of pre-summer rainfall over south China and associated synoptic conditions. *Journal of the Meteorological Society of Japan, Ser. II*, *98*, 213–233. https://doi.org/10.2151/jmsj.2020-012

Lin, L. X., Feng, Y. R., & Huang, Z. (2006). *Technical guidance on weather forecasting in Guangdong Province (in Chinese)* (pp. 143–152). China Meteorological Press.

Liu, X., Luo, Y., Guan, Z., & Zhang, D.-L. (2018). An extreme rainfall event in coastal South China during SCMREX-2014: Formation and roles of rainband and echo trainings. *Journal of Geophysical Research - D: Atmospheres*, *123*, 9256–9278. https://doi.org/10.1029/2018jd028418

Liu, X., Luo, Y., Zhang, D.-L., & Guan, Z. (2020). Roles of double low-level jets in the generation of coexisting inland and coastal heavy rainfall over South China during the presummer rainy season. *Journal of Geophysical Research - D: Atmospheres*, *125*, e2020JD032890. https://doi.org/10.1029/2020jd032890

Liu, X. T., Wan, Q. L., Wang, H., Xiao, H., Zhang, Y., Zheng, T., & Feng, L. (2018). Raindrop size distribution parameters retrieved from Guangzhou S-band polarimetric radar observations. *Journal of Meteorological Research*, *32*(4), 571–583. https://doi.org/10.1007/s13351-018-7152-4

Luo, Y., Xia, R., & Chan, J. C. L. (2020). Characteristics, physical mechanisms, and prediction of pre-summer rainfall over South China: Research progress during 2008-2019. *Journal of the Meteorological Society of Japan*, *98*, 19–42. https://doi.org/10.2151/jmsj.2020-002

Luo, Y., Zhang, R., Wan, Q., Wang, B., Wong, W. K., Hu, Z., et al. (2017). The Southern China Monsoon Rainfall Experiment (SCMREX). *Bulletin of the American Meteorological Society*, *98*, 999–1013. https://doi.org/10.1175/bams-d-15-00235.1

Matsui, T., Dolan, B., Iguchi, T., Rutledge, S. A., Tao, W.-K., & Lang, S. (2020). Polarimetric radar characteristics of simulated and observed intense convective cores for a midlatitude continental and tropical maritime environment. *Journal of Hydrometeorology*, *21*, 501–517. https://doi.org/10.1175/jhm-d-19-0185.1

Nielsen, E. R., & Schumacher, R. S. (2018). Dynamical insights into extreme short-term precipitation associated with supercells and mesovortices. *Journal of the Atmospheric Sciences*, *75*, 2983–3009. https://doi.org/10.1175/jas-d-17-0385.1

Nielsen, E. R., & Schumacher, R. S. (2020). Dynamical mechanisms supporting extreme rainfall accumulations in the Houston "Tax Day" 2016 Flood. *Journal of the Atmospheric Sciences*, *148*, 83–109. https://doi.org/10.1175/mwr-d-19-0206.1

Park, H., Ryzhkov, A., Zrnic, D., & Kim, K. (2009). The hydrometeor classification algorithm for the polarimetric WSR-88D: Description and application to an MCS. *Weather and Forecasting*, *24*, 730–748. https://doi.org/10.1175/2008waf2222205.1

Rosenfeld, D., Lohmann, U., Raga, G., O'Dowd, C., Kulmala, M., Fuzzi, S., et al. (2008). Floor or drought: How do aerosols affect precipitation? *Science*, *321*, 1309–1313. https://doi.org/10.1126/science.1160606

Rowe, A., Rutledge, S., & Lang, T. (2011). Investigation of microphysical processes occurring in isolated convection during NAME. *Monthly Weather Review*, *139*, 424–443. https://doi.org/10.1175/2010mwr3494.1

Rowe, A., Rutledge, S., & Lang, T. (2012). Investigation of microphysical processes occurring in organized convection during NAME. *Monthly Weather Review*, *140*, 2168–2187. https://doi.org/10.1175/mwr-d-11-00124.1

Tan, J., Huffman, G. J., Bolvin, D. T., & Nelkin, E. J. (2019). IMERG V06: Changes to the morphing algorithm. *Journal of Atmospheric and Oceanic Technology*, *36*(12), 2471–2482. https://doi.org/10.1175/jtech-d-19-0114.1

Tao, S., & Chen, L. (1987). A review of recent research on the East Asian summer monsoon in China. In C.-P. Chang, & T. N. Krishnamurti (Eds.), *Monsoon meteorology* (pp. 60–92). Oxford University Press.

Testud, J., Oury, S., Amayenc, P., Black, R. A., & Dou, X. (2001). The concept of "normalized" distributions to describe raindrop spectra: A tool for cloud physics and cloud remote sensing. *Journal of Applied Meteorology*, *40*, 1118–1140. https://doi.org/10.1175/1520-0450(2001)040<1118:tcondt>2.0.co;2

Ulbrich, C. W. (1983). Natural variations in the analytical form of the raindrop size distribution. *Journal of Applied Meteorology*, *22*, 1764–1775. https://doi.org/10.1175/1520-0450(1983)022<1764:nvitaf>2.0.co;2

Ulbrich, C. W., & Atlas, D. (2007). Microphysics of raindrop size spectra: Tropical continental and maritime storms. *Journal of Applied Meteorology and Climatology*, *46*, 1777–1791. https://doi.org/10.1175/2007jamc1649.1

Wang, H., Kong, F., Wu, N., Lan, H., & Yin, J. (2019). An investigation into microphysical structure of a squall line in South China observed with a polarimetric radar and a disdrometer. *Atmospheric Research*, *226*, 171–180. https://doi.org/10.1016/j.atmosres.2019.04.009

Wang, H., Luo, Y., & Jou, B. (2014). Initiation, maintenance, and properties of convection in an extreme rainfall event during SCMREX: Observational analysis. *Journal of Geophysical Research - D: Atmospheres*, *119*, 13. https://doi.org/10.1002/2014jd022339

Wen, J., Zhao, K., Huang, H., Zhou, B., Yang, Z., Chen, G., et al. (2017). Evolution of microphysical structure of a subtropical squall line observed by a polarimetric radar and a disdrometer during OPACC in Eastern China. *Journal of Geophysical Research - D: Atmospheres*, *122*, 8033–8050. https://doi.org/10.1002/2016jd026346

Wu, C., Liu, L., Wei, M., Xi, B., & Yu, M. (2018). Statistics-based optimization of the polarimetric radar hydrometeor classification algorithm and its application for a squall line in South China. *Advances in Atmospheric Sciences*, *35*, 296–316. https://doi.org/10.1007/s00376-017-6241-0

Wu, D., Zhao, K., Kumjian, M. R., Chen, X., Huang, H., Wang, M., et al. (2018). Kinematics and microphysics of convection in the outer rainband of Typhoon Nida (2016) revealed by polarimetric radar. *Monthly Weather Review*, *146*, 2147–2159. https://doi.org/10.1175/mwr-d-17-0320.1

Wu, M., & Luo, Y. (2016). Mesoscale observational analysis of lifting mechanism of a warm-sector convective system producing the maximal daily precipitation in China mainland during pre-summer rainy season of 2015. *Journal of Meteorological Research*, *30*, 719–736. https://doi.org/10.1007/s13351-016-6089-8

Wu, N., Ding, X., Wen, Z., Chen, G., Meng, Z., Lin, L., & Min, J. (2020). Contrasting frontal and warm-sector heavy rainfalls over South China during the early-summer rainy season. *Atmospheric Research*, *235*(10), 4693. https://doi.org/10.1016/j.atmosres.2019.104693

Xia, R., Zhao, S., & Sun, J. (2006). Analysis and study on environment characteristics of the Class-1 β mesoscale system in the warm sector ahead of front in South China (in Chinese). *Atmospheric Sciences*, *30*, 988–1007.

Xu, W., & Zipser, E. J. (2015). Convective intensity, vertical precipitation structures, and microphysics of two contrasting convective regimes during the 2008 TiMREX. *Journal of Geophysical Research - D: Atmospheres*, *120*, 4000–4016. https://doi.org/10.1002/2014jd022927

Xu, W., Zipser, E. J., & Liu, C. (2009). Rainfall characteristics and convective properties of mei-yu precipitation systems over South China, Taiwan and the South China Sea. Part I: TRMM observations. *Monthly Weather Review*, *137*, 4261–4275. https://doi.org/10.1175/2009mwr2982.1

Zhang, G. F., Vivekanandan, J., & Brandes, E. A. (2001). A method for estimating rain rate and drop size distribution from polarimetric radar measurements. *IEEE Transactions on Geoscience and Remote Sensing*, *39*, 830–841. https://doi.org/10.1109/36.917906

Zhang, G. F., Vivekanandan, J., Brandes, E. A., Meneghini, R., & Kozu, T. (2003). The shape-slope relation in observed Gamma raindrop size distributions: Statistical error or useful information? *Journal of Atmospheric and Oceanic Technology*, *20*, 1106–1119. https://doi.org/10.1175/1520-0426(2003)020<1106:tsriog>2.0.co;2

Zhang, J., Howard, K., & Gourley, J. J. (2005). Constructing three-dimensional multiple-radar reflectivity mosaics: Examples of convective storms and stratiform rain echoes. *Journal of Atmospheric and Oceanic Technology*, *22*, 30–42. https://doi.org/10.1175/jtech-1689.1

Zhang, R., Ni, Y., Liu, L., Luo, Y., & Wang, Y. (2011). South China Heavy Rainfall Experiments (SCHeREX). *Journal of the Meteorological Society of Japan*, *89A*, 153–166. https://doi.org/10.2151/jmsj.2011-a10

Zhao, K., Huang, H., Wang, M., Lee, W.-C., Chen, G., Wen, L., et al. (2019). Recent progress in dual-polarization radar research and applications in China. *Advances in Atmospheric Sciences*, *36*, 961–974. https://doi.org/10.1007/s00376-019-9057-2

Zhao, S. X., Bei, N. F., & Sun, J. H. (2007). Mesoscale analysis of a heavy rainfall event over Hong Kong during a pre-rainy season in South China. *Advances in Atmospheric Sciences*, *24*, 555–572. https://doi.org/10.1007/s00376-007-0555-2

Zhou, X. J., et al. (2003). *Heavy rainfall experiment in South China during pre-rainy season (HUAMEX), 1998 (in Chinese)*, (p. 220). China Meteorological Press.

Zipser, E., Liu, C., Cecil, D., Nesbitt, S. W., & Yorty, S. (2006). Where are the most intense thunderstorms on Earth? *Bulletin of the American Meteorological Society*, *87*, 1057–1072. https://doi.org/10.1175/bams-87-8-1057

Zipser, E. J., & Lutz, K. R. (1994). The vertical profile of radar reflectivity of convective cells: A strong indicator of storm intensity and lightning probability? *Monthly Weather Review*, *122*, 1751–1759. https://doi.org/10.1175/1520-0493(1994)122<1751:tvporr>2.0.co;2

Zrnic, D., & Ryzhkov, A. (1999). Polarimetry for weather surveillance radars. *Bulletin of the American Meteorological Society*, *80*, 389–406. https://doi.org/10.1175/1520-0477(1999)080<0389:pfwsr>2.0.co;2